Equilibrium inter-mineral titanium isotope fractionation: Implication for high-temperature titanium isotope geochemistry

Wenzhong Wang[a,*], Shichun Huang[b], Fang Huang[c], Xinmiao Zhao[d], Zhongqing Wu[a,*]

[a] Laboratory of Seismology and Physics of Earth's Interior, School of Earth and Space Sciences, University of Science and Technology of China, Hefei, Anhui 230026, China

[b] Department of Geoscience, University of Nevada, Las Vegas, NV 89154, United States

[c] CAS Key Laboratory of Crust-Mantle Materials and Environments, School of Earth and Space Sciences, University of Science and Technology of China, Hefei, Anhui 230026, China

[d] State Key Laboratory of Lithospheric Evolution, Institute of Geology and Geophysics, Chinese Academy of Sciences, Beijing 100029, China

5696 words, 5 figures, 3 tables, and supplementary materials

[*] Correspondences and requests for materials should be addressed to Wenzhong Wang (wz30304@mail.ustc.edu.cn) or Zhongqing Wu (wuzq10@ustc.edu.cn)

Abstract

Equilibrium Ti isotope fractionation factors among major Ti-bearing minerals are critical for understanding Ti isotope fractionation during magmatic processes. We use the first-principles calculations based on the density functional theory (DFT) to obtain Ti isotope reduced partition function ratios ($10^3 \ln\beta$ of $^{49}Ti/^{47}Ti$) in a series of important Ti bearing minerals, including Ti-doped clinopyroxene, orthopyroxene, olivine, and pyrope, geikielite-ilmenite solid solutions, and rutile. There is a large variation in our calculated $10^3 \ln\beta$, which are linearly correlated to their Ti force constants, a parameter related to the average Ti-O bond length and the Ti valence state. Among all studied minerals, silicates with Ti^{4+} occupying the tetrahedral Si site have the highest $10^3 \ln\beta$, and rutile has the lowest $10^3 \ln\beta$. The valence state also significantly controls the $10^3 \ln\beta$. Typically, Ti^{3+}-doped silicates have lower $10^3 \ln\beta$ than those of Ti^{4+}-doped silicates. At the natural abundance levels, the $10^3 \ln\beta$ of Ti^{4+}_{Si}-doped and Ti^{3+}_{Mg}-doped (Ti^{3+} occupying the Mg site) silicate minerals show no concentration effect. That is, their $10^3 \ln\beta$ do not vary with their Ti^{4+} and Ti^{3+} contents, respectively. In contrast, the $10^3 \ln\beta$ of geikielite-ilmenite solutions significantly decrease with increasing Fe/(Fe+Mg) ratio.

Our calculations predict no significant Ti isotope fractionation among Ti^{4+}_{Si}-doped clinopyroxene, orthopyroxene, olivine, and pyrope (< 0.08 % at 1200 K), whereas the $10^3 \ln\alpha$ between geikielite-ilmenite solutions and Ti^{4+}_{Si}-doped clinopyroxene ranges from ~-0.67‰ to -0.49‰ at 1200 K, supporting the hypothesis

that Fe-Ti oxides are important fractionating Ti isotopes during magma differentiation. Finally, the large equilibrium Ti isotope fractionation between geikielite-ilmenite solutions and clinopyroxene suggests that Ti isotopes can be used as a thermometer with precision comparable to that of elemental geothermometer.

Keywords: Ti isotopes; First-principle calculations; Fe-Ti oxides; silicate minerals; Equilibrium fractionation factors; Magma differentiation.

1. Introduction

Titanium (Ti) is an important rock-forming element in terrestrial planets (Anders and Grevesse, 1989; McDonough and Sun, 1995). It is lithophile, incompatible, and fluid-immobile, and it has been extensively used in high-temperature geochemistry. For example, the temperature dependent Ti solubility in quartz and zircon have been widely used as geothermometers (e.g., Watson et al., 2006; Wark and Watson, 2006). Titanium is also a highly refractory element (Lodders, 2003), playing an important role in our understanding of refractory inclusions in chondrites (e.g., Simon et al., 2007; Simon et al., 2017; Davis et al., 2018). In terrestrial rocks, Ti is usually present as Ti^{4+}. Significant amounts of Ti^{3+} could be present under extremely reduced conditions such as in lunar rocks and refractory inclusions (Simon et al., 2007; Simon and Sutton, 2017), and thus the Ti^{3+}/Ti^{4+} ratio can be used for measuring oxygen fugacity (e.g., Simon et al., 2007).

Titanium has five stable isotopes, ranging from ^{46}Ti (8.25%) to ^{50}Ti (5.18%). With the advancement in analytical techniques, Ti isotope composition has become an important cosmochemical and geochemical tracer (e.g., Leya et al., 2008, 2009; Trinquier et al., 2009; Zhang et al., 2011, 2012, 2014; Millet and Dauphas, 2014; Kööp et al., 2016a, b; Williams et al., 2016; Greber et al., 2017a, b; Simon et al., 2017; Davis et al., 2018; Deng et al., 2018a, b, 2019). For example, both mass-dependent and mass-independent Ti isotope variations have been reported in meteorites and their components, which are used to constrain the origin and evolution of early solar

system (Simon et al., 2017; Greber et al., 2017a; Davis et al., 2018; Deng et al., 2018a).

Titanium isotope composition can be also used to trace magma differentiation processes. Large mass-dependent Ti isotope variation, $\delta^{49}Ti$ ranging from −0.01 ± 0.03‰ to +2.01 ± 0.01‰ ($\delta^{49}Ti = [(^{49}Ti/^{47}Ti)_{sample} / (^{49}Ti/^{47}Ti)_{standard} - 1]*1000$ ‰), is observed in terrestrial rocks (Millet et al., 2016; Greber et al., 2017b; Deng et al., 2018b, 2019), which is thought to reflect Fe-Ti oxides fractionation during magma evolution. Specifically, Millet et al. (2016) found that $\delta^{49}Ti$ is positively correlated with SiO_2 content in differentiated terrestrial rocks, inferring that Fe-Ti oxides are enriched in light Ti isotopes relative to the melt. Using additional data from plume-related volcanoes (Hekla from Iceland, and Afar), Deng et al. (2019) identified two $\delta^{49}Ti$ vs. SiO_2 content trends, one defined by plume lavas and another by arc settings lavas. They argued that this is because the high Ti melt contents in plume lavas due to both high initial TiO_2 contents and delayed onset of Fe-Ti oxides from low oxygen fugacity drive the larger Ti isotope fractionation seen in plume lavas relative to arc setting lavas. Best fit for the relationship between $\delta^{49}Ti$ and f_{Ti}, the Ti proportion remaining in the melt, indicates that Ti isotope behaviors are controlled by the fractional crystallization of Ti-Fe oxides (such as ilmenite and titanomagnetite). In addition, Millet et al. (2016) also found that high-Ti lunar basalts have relatively higher $\delta^{49}Ti$ values than low-Ti mare basalts, which was ascribed to the Ti isotope fractionation induced by ilmenite (Millet et al., 2016). In igneous rocks, Fe-Ti oxides

88 are major hosts of Ti, which can be also incorporated into silicate minerals as a minor
89 element. The equilibrium Ti isotope fractionation factors among major Ti-oxides and
90 silicate minerals are important in understanding the reported δ^{49}Ti variations in both
91 terrestrial and lunar rocks. However, such data do not exist in the literature.

92 Due to the difficulty and uncertainty to reach the isotope exchange equilibrium
93 among minerals inside experiment charges, experimental determinations of
94 inter-mineral equilibrium isotope fractionation at high temperature are still
95 challenging. First-principles calculations based on the density functional theory (DFT)
96 predict inter-mineral isotope fractionation factors with accuracy and precision
97 comparable to some of the well-designed experiments (Lejaeghere et al., 2016). This
98 technique has been widely used to calculate equilibrium isotope fractionation in many
99 systems (e.g., Méheut et al., 2009; Rustad and Yin, 2009; Schauble, 2011; Li and Liu,
100 2011; Fujii et al., 2011; Huang et al., 2013; Feng et al., 2014; Wang, et al., 2017a, b;
101 Liu et al., 2018; Huang et al., 2019; Li et al., 2019).

102 Here we investigated the equilibrium inter-mineral Ti isotope fractionation
103 factors among Ti-doped clinopyroxene (clinopyroxene), orthopyroxene
104 (orthopyroxene), olivine, and pyrope, geikielite-ilmenite solid solutions, and rutile
105 using first-principles calculations based on the DFT. Ti is a minor element in silicate
106 minerals and the Ti contents in pyroxenes, olivine, and garnet vary significantly (e.g.,
107 Hermann et al., 2005; Gerke et al., 2005). Although Ti^{3+} does not occur in terrestrial
108 rocks, it is present in lunar rocks and refractory inclusions in chondrites (e.g., Simon

et al., 2007; Simon and Sutton, 2017), which were produced under extremely reducing conditions. Thus, both Ti^{4+}-doped and Ti^{3+}-doped silicate minerals are considered in this work. More importantly, because of mineral concentration effect on the equilibrium isotope fractionation (Feng et al., 2014; Wang et al., 2017a, b; Li et al., 2019), we also investigated the effect of silicate mineral Ti concentration on the equilibrium inter-mineral Ti isotope fractionation factors. This study for the first time provides fundamental equilibrium inter-mineral fractionation data to understand the Ti isotope behaviors during magmatic and metamorphic processes.

2. Calculation methods

2.1 Equilibrium isotope fractionation factor

According to Urey (1947), the isotopic substitution of a specific element in two phases would induce a difference in vibrational frequency properties, which results in mass-dependent equilibrium isotope fractionation between these two phases. Following Richet et al. (1977), the reduced partition function ratio β_A of the element X in phase A is the X isotope fractionation factor between the phase A and an ideal atomic gas. Based on the harmonic approximation, β_A can be written as:

$$\beta_A = \frac{Q_h}{Q_l} = \prod_i^{3N} \frac{u_{ih}}{u_{il}} \frac{e^{-\frac{1}{2}u_{ih}}}{1-e^{-u_{ih}}} \frac{1-e^{-u_{il}}}{e^{-\frac{1}{2}u_{il}}} \quad (1)$$

where *h* and *l* refer to the heavy and light isotopes, respectively, running index *i* refers to the i^{th} vibrational frequency, and *N* is the number of atoms in the unit cell. A phase with *N* atoms has *3N* vibrational modes and thus the product runs over all *3N* phonon

modes. Q_h and Q_l represent the vibrational partition function for the heavy and light isotopes, respectively. u_{ih} and u_{il} are defined as:

$$u_{ih\ or\ il} = \hbar\omega_{ih\ or\ il}/k_B T \quad (2)$$

where $\hbar$ and k_B are the Planck and Boltzmann constants, respectively, T is temperature in Kelvin, and $\omega_{ih\ or\ il}$ is the vibrational frequency of the i^{th} mode. Consequently, the equilibrium isotope fractionation factor between Phases A and B can be expressed as:

$$\Delta_{A-B} \approx 10^3 ln\alpha_{A-B} = 10^3 ln\beta_A - 10^3 ln\beta_B \quad (3)$$

2.2 First-principles calculations

We performed first-principles calculations using the software "Quantum Espresso" (Giannozzi et al., 2009), which is based on the DFT, plane wave, and pseudopotential, following a procedure similar to our previous studies (Huang et al., 2013; Feng et al., 2014; Wu et al., 2015; Wang et al., 2017a, b; Qian et al., 2018; Wang and Wu, 2018; Li et al., 2019). We adopted the local density approximation (LDA) (Perdew and Zunger, 1981) to describe the exchange correlation functional. The pseudopotentials of Mg, Ca, Si, Al, and O used in this study are the same as the ones used in our previous work (Huang et al., 2013; Feng et al., 2014; Wang et al., 2017b; Wang and Wu, 2018). The pseudopotentials of Ti and Fe were generated using the Vanderbilt method (Vanderbilt, 1990) with a valence configuration of $3s^2 3p^6 4s^2 3d^2$ and a cutoff radii of 1.8 Bohr for Ti, and $3s^2 3p^6 3d^{6.5} 4s^1 4p^0$ and 1.8 Bohr for Fe. In order to describe the large on-site Coulomb interactions among the localized electrons

151 (*3d* electrons of Fe and Ti) (Anisimov et al., 1991), we introduced a Hubbard U
152 correction to the LDA for all DFT calculations (LDA+U). Hubbard U values for Fe
153 and Ti atoms on different sites in all calculated minerals (Table S1) were
154 non-empirically determined using the linear response method (Cococcioni and de
155 Gironcoli, 2005).

156 We first optimized all crystal structures of Ti-bearing minerals using the variable
157 cell shape molecular dynamics method (Wentzcovitch, 1991) with different k-point
158 grids according to their unit cell sizes (see Table S1). The energy cutoff for plane
159 wave and charge density are set to 70 Ry and 700 Ry, respectively. The residual forces
160 converge within 10^{-4} Ry/Bohr. After the relaxed structures were obtained, we then
161 calculated phonon vibrational frequencies using the finite displacement method as
162 implemented in the open-source code PHONOPY (Togo and Tanaka, 2015). To make
163 comparisons of compare transverse-optical and longitudinal-optical frequencies of
164 rutile between theoretical predictions and experimental measurements, we also
165 calculated its vibrational frequencies based on the density-functional perturbation
166 theory (DFPT), which includes the effects of dielectric tensors and effective charges.
167 Hereafter all phonon calculations are based on the finite displacement method unless
168 specially mentioned. The reduced partition function ratios β of $^{49}Ti/^{47}Ti$ for all
169 calculated minerals can be obtained using Eq. (1). The finite displacement method and
170 DFPT give the similar β factor of rutile.

171 Some previous studies also performed DFT+U calculations to predict the

electronic structure and optical properties of TiO_2 polymorphs. For example, Gao et al. (2006) suggested that V-doped rutile TiO_2 is a half-metal within LDA while a semiconductor within the LDA+U. The DFT + U method has been also applied in Ti 3d of TiO_2 by Arroyo-De Dompablo et al. (2011) to improve the accuracy of standard DFT. Portillo-Vélez et al. (2013) also investigated the influence of surface oxygen vacancies in the structural and electronic properties of anatase TiO_2 (1 0 1) surface using Hubbard U correction. Curnan and Kitchin (2015) also performed a DFT+U study about the relative energetic ordering of rutile, anatase, brookite and columbite TiO_2 polymorphs. A recent study reported by Samat et al. (2016) also investigated the optical properties of titanium dioxide (TiO_2) in rutile, anatase and brookite phases via DFT+U calculations.

In order to check the effect of Hubbard U correction, we also performed LDA calculations for rutile, geikielite, clinopyroxene ($Mg_8Ca_8Si_{15}TiO_{48}$), and orthopyroxene ($Mg_{16}Si_{15}TiO_{48}$). The LDA results are compared to LDA+U results in Table S6-S7 and Figure S1-S2. The LDA predicts smaller static volumes and shorter average Ti-O bond lengths than LDA+U (Table S6). Both LDA and LDA+U underestimate mineral volumes at static conditions, but the ones calculated within LDA+U are closer to experimental values. When we considered the effects of zero-point motion and room temperature on volumes, the equation of states of rutile and geikielite calculated within LDA+U show great agreements with experimental measurements at 300 K (Fig. S3 and S4), revealing the validity of +U correction.

193 Unexpectedly, we find that LDA gives some negative frequencies for rutile (Fig. S1),
194 while LDA+U calculations predict normal phonon frequencies that are generally in
195 agreements with experimental measurements (Table S5). Thus, we cannot obtain the
196 $10^3 \ln\beta$ of rutile and its volume-pressure relationship from LDA calculations. For
197 clinopyroxene ($Mg_8Ca_8Si_{15}TiO_{48}$), and orthopyroxene ($Mg_{16}Si_{15}TiO_{48}$), LDA gives
198 larger $10^3 \ln\beta$ values than LDA+U (Table S6 and S7) because LDA predicts shorter
199 average Ti-O bond lengths than LDA+U (Table S6). However, the $10^3 \ln\alpha$ between
200 clinopyroxene and orthopyroxene from LDA calculations are similar to the one from
201 LDA+U calculations (0.02 ‰ for LDA+U vs. 0.03 ‰ for LDA at 1000 K). For
202 geikielite, +U correction shows a mild effect on vibrational frequencies (Fig. S2), and
203 the average Ti-O bond length and $10^3 \ln\beta$ calculated within LDA are only slightly
204 shorter and larger than those predicted by LDA+U (Table S6), respectively. Therefore,
205 we focus on the results calculated within LDA+U thereafter.
206
207 **3. Results**
208 **3.1 Ti incorporation into major silicate minerals**
209 Ti is a minor element in the major silicate minerals, such as olivine,
210 clinopyroxene, orthopyroxene, and garnet. The amount of TiO_2 in olivine is usually
211 lower than 1.0 wt% (Hermann et al., 2005), while pyroxenes and garnet can dissolve
212 up to several weight percent of TiO_2 (Gerke et al., 2005). Although major element
213 sites in these silicate minerals are well known, potential Ti substitution mechanisms

214 are pretty complicated and some are still under debate. In Ti-doped olivine, Ti is
215 negatively correlated with Si, but there is no correlation between Ti and Mg contents
216 (Hermann et al., 2005). This implies that Ti mainly substitutes for Si in the olivine
217 tetrahedral sites (Hermann et al., 2005; Berry et al., 2007). Simon et al. (2007; 2016)
218 reported both Ti^{3+} and Ti^{4+} in lunar pyroxenes, with Ti^{4+} preferentially occupying the
219 tetrahedral Si site and Ti^{3+} occupying the octahedral Mg position (M1) (Skogby et al.,
220 2006). Notably, Ti^{3+} only appears in some lunar pyroxenes produced under extremely
221 reducing conditions (Simon and Sutton, 2017), whereas there is no measurable Ti^{3+} in
222 terrestrial rocks. Garnet has a generalized chemical formula of $X^{2+}{}_3Y^{3+}{}_2Z^{4+}{}_3O_{12}$,
223 where X^{2+}, Y^{3+}, and Z^{4+} occupy the dodecahedral, octahedral, and tetrahedral sites,
224 respectively. In the upper mantle, garnet is mainly made of its Mg-Al end-member
225 pyrope ($Mg_3Al_2Si_3O_{12}$). Several substitution mechanisms have been proposed to
226 incorporate Ti into garnet, which can be divided into two types of site occupancies
227 (Ackerson et al., 2017). In one type, Ti^{4+} occupies the tetrahedral Z site through a
228 simple $Si^{4+}\leftrightarrow Ti^{4+}$ substitution (Armbruster and Geiger, 1993; Gwalani et al., 2000). In
229 the other type, Ti^{4+} occupies the octahedral Y site through a paired cation substitution,
230 such as $^{VI}Al^{3+}+{}^{IV}Si^{4+}\leftrightarrow{}^{VI}Ti^{4+}+{}^{IV}Al^{3+}$, to balance the charge (Grew et al., 2013; Proyer
231 et al., 2013; Ackerson et al., 2017). Under extremely reducing environment, Ti^{3+} can
232 be also directly incorporated into the octahedral Y site; however, terrestrial garnets
233 contains negligible amount of Ti^{3+} (Gwalani et al., 2000; Grew et al., 2013).
234 Consequently, Ti^{3+} is irrelevant to terrestrial rocks, and will not be further discussed in

235 the topic relevant to terrestrial rocks.

236 Here we investigated the configuration when Ti^{4+} occupies the tetrahedral Si site
237 in olivine, orthopyroxene, clinopyroxene, and pyrope through the $Si^{4+} \leftrightarrow Ti^{4+}$
238 substitution. Orthopyroxene has two nonequivalent tetrahedral Si sites, SiA and SiB.
239 Our calculations show that the energy difference between Ti^{4+} in the SiA and SiB sites
240 is large, 0.39 eV for orthopyroxene with Ti/(Ti+Si)=1/32, suggesting that Ti^{4+} prefers
241 the SiB site. Thus, orthopyroxene with Ti^{4+} occupying the SiB site was used in our
242 calculations. We also calculated the Ti-doped pyrope generated by coupled
243 substitution, $^{VI}Al^{3+}+^{IV}Si^{4+} \leftrightarrow ^{VI}Ti^{4+}+^{IV}Al^{3+}$. Particularly, Ti^{4+} occupies the octahedral
244 Al site, and the original Al^{3+} now occupies the nearest tetrahedral Si site. This
245 substitution mechanism yields several nonequivalent configurations. All
246 nonequivalent structures were investigated, and our calculations show the energy
247 difference between other nonequivalent structures and the one with the lowest total
248 energy is also large (i.e., > 0.21 eV for $Mg_{24}Al_{15}TiSi_{23}AlO_{96}$ pyrope). Similarly,
249 the structure with the lowest total energy was used. Our calculations show that the
250 energy difference between two Ti^{4+}-doped pyrope structures generated through two
251 different substitution mechanisms ($^{VI}Al^{3+}+^{IV}Si^{4+} \leftrightarrow ^{VI}Ti^{4+}+^{IV}Al^{3+}$ and $Si^{4+} \leftrightarrow Ti^{4+}$) is
252 very small (i.e., ~0.02 eV between $Mg_{24}Al_{15}TiSi_{23}AlO_{96}$ and $Mg_{24}Al_{16}TiSi_{23}O_{96}$
253 pyrope), suggesting these two substitution mechanisms are equally important for the
254 incorporation of Ti^{4+} into pyrope.

255 The Ti^{3+} incorporation into orthopyroxene and clinopyroxene through the

256 $^{VI}Mg^{2+}+^{IV}Si^{4+}\leftrightarrow{}^{VI}Ti^{3+}+^{IV}Al^{3+}$ substitution (Simon and Sutton, 2017) and into pyrope
257 through $^{VI}Al^{3+}\leftrightarrow{}^{VI}Ti^{3+}$ were also investigated. Orthopyroxene has two nonequivalent
258 Mg sites (M1 and M2). The configuration that M1-site Mg and its nearest SiB-site Si
259 are replaced by Ti and Al atoms respectively has the lowest total energy. Similarly, the
260 Ti-doped clinopyroxene generated by replacing the nearest neighbor $^{VI}Mg^{2+}$–$^{IV}Si^{4+}$
261 pair with $^{VI}Ti^{3+}$–$^{IV}Al^{3+}$ pair is the most stable one.

262 Finally, because naturally occurring silicate minerals have variable Ti contents,
263 we also calculated the structures and reduced partition function ratios of these
264 Ti-doped silicate minerals with different Ti contents. The initial structures of
265 clinopyroxene, orthopyroxene, olivine, and pyrope with different Ti contents were
266 obtained by incorporating Ti into their supercells, which were generated by expanding
267 the primitive cell along different directions. For example, the 80-atom and 320-atom
268 supercells of clinopyroxene could be obtained by expanding the primitive cell twice
269 along the c direction and twice simultaneously along a, b, c directions, respectively.
270 Substituting one Si atom with one Ti atom can produce the initial clinopyroxene
271 structures with Ti/(Ti+Si) of 1/16 and 1/64, respectively. Similarly, replacing the
272 nearest neighboring $^{VI}Mg^{2+}$–$^{IV}Si^{4+}$ pair in an 80-atom clinopyroxene supercell with
273 $^{VI}Ti^{3+}$–$^{IV}Al^{3+}$ pair could generate the initial configuration with Ti/(Ti+Si)=1/16 for the
274 $^{VI}Mg^{2+}+^{IV}Si^{4+}\leftrightarrow{}^{VI}Ti^{3+}+^{IV}Al^{3+}$ substitution. Initial structures of other minerals were
275 also produced in the same way. The supercell construction details are shown in Table
276 1.

3.2 Relaxed crystal structures

All relaxed structures of Ti-doped silicate minerals and Fe-Ti oxides, including geikielite-ilmenite solid solutions and rutile, are shown in Fig. 1 with emphases on Mg-O, Ca-O, Fe-O, Si-O, Ti-O, and Al-O polyhedrons. Their atomic positions can be found in the supplementary materials. The relaxed cell parameters are reported in Table S2. Cell parameters and volumes of geikielite, ilmenite, and rutile calculated based on LDA at static conditions agree with experimental data at 300 K within 2% (Table S2). Typically, the LDA calculation at static conditions underestimates the volume by ~1-2% because the effects of zero-point motion and room temperature on volumes have not been considered. When these effects are taken into account, the theoretical results for orthopyroxene, clinopyroxene, olivine, and pyrope are consistent with experimental data within 1% (Huang et al., 2013; Huang et al., 2014; Wu et al., 2015). There is no experimental measurement of the volumes of Ti-doped silicate minerals. Moreover, most calculated vibrational frequencies for geikielite, $FeTiO_3$ ilmenite, and rutile are also in agreements with experimental results (Table S3-S5), although some calculated frequencies significantly deviate from experimental data. These comparisons justify the reliability and accuracy of our calculations. Following Méheut et al. (2009), the uncertainty on $10^3 \ln\beta$ and $10^3 \ln\alpha$ is 3.6% and 5.0%, respectively, which are estimated based on the relationship between the calculated and measured frequencies for pure silicate minerals and Fe-Ti oxides (Table S3-S5, Huang et al., 2013).

298 **3.3 Average Ti-O bond lengths**

299 The calculated average Ti-O bond lengths and Ti coordination numbers (CNs) in
300 Ti-doped silicate minerals, geikielite-ilmenite solid solutions, and rutile are listed in
301 Table 1. The average Ti-O bond length and Ti CN depend on the arbitrarily accepted
302 threshold of Ti-O bond lengths. Because Ti-O distances in all calculated minerals
303 form two populations, ranging from 1.7 Å to 2.2 Å or greater than 3.0 Å, we adopted
304 the value of 2.2 Å as the cutoff to determine Ti-O bond lengths and Ti CNs. In all
305 silicate minerals, Ti occupying the tetrahedral Si site has a CN of four. Titanium,
306 either Ti^{3+} or Ti^{4+}, occupying the octahedral Mg site in pyroxenes and the octahedral
307 Al site in pyrope has a CN of 6. In Fe-Ti oxides, Ti has a CN of 6.

308 Ti^{4+} occupying the tetrahedral Si site in clinopyroxene, orthopyroxene, olivine,
309 and pyrope through the $Si^{4+}\leftrightarrow Ti^{4+}$ substitution have similar average Ti-O bond
310 lengths, which are the shortest among all calculated minerals. In contrast, Ti^{3+}
311 occupying the octahedral Mg site in pyroxenes through the $Mg^{2+}+Si^{4+}\leftrightarrow Ti^{3+}+Al^{3+}$
312 substitution has the longest average Ti-O bond length. Both Ti^{4+} and Ti^{3+} can occupy
313 the octahedral Al site in pyrope through $Al^{3+}+Si^{4+}\leftrightarrow Ti^{4+}+Al^{3+}$ and $Al^{3+}\leftrightarrow Ti^{3+}$
314 substitutions, respectively, but the average Ti^{4+}-O bond is significantly shorter than
315 that of Ti^{3+}-O. The average Ti-O bond length increases in the order of: Ti^{4+}-O in
316 silicates < Ti^{4+}-O in Fe-Ti oxides < Ti^{3+}-O in silicates.

317 Within the explored compositional space (Table 1), there is no significant Ti^{4+} or
318 Ti^{3+} concentration effect on the average Ti-O bond lengths (< 0.02 Å) in silicate

minerals. In contrast, Mg or Fe concentration affect the average Ti-O bond lengths in geikielite-ilmenite solutions, from 1.9685 Å in $MgTiO_3$ to 1.9733 Å in $FeTiO_3$.

3.4 The reduced partition function ratios (10^3lnβ) of $^{49}Ti/^{47}Ti$

The 10^3lnβ of $^{49}Ti/^{47}Ti$ of all calculated minerals are shown in Fig. 2, and their polynomial fitting factors as a function of temperature are listed in Table 2. The 10^3lnβ are described using the following five categories: (1) Ti^{4+}_{Si}: Ti^{4+} occupies the tetrahedral site in pyroxenes, olivine, and pyrope; (2) Ti^{4+}_{Al}: Ti^{4+} occupies the octahedral Al site in pyrope; (3) Ti^{3+}_{Al}: Ti^{3+} occupies the octahedral Al site in pyrope; (4) Fe-Ti oxides, including geikielite-ilmenite solutions and rutile; (5) Ti^{3+}_{Mg}: Ti^{3+} occupies the octahedral Mg site in pyroxenes, olivine, and pyrope. At 1000 K, the 10^3lnβ ranges from 2.29 ‰ in Ti^{4+}_{Si}-doped olivine to 1.18 ‰ in rutile (Table 2). It decreases in the order of Ti^{4+}_{Si}-doped olivine, clinopyroxene, orthopyroxene, and pyrope > Ti^{4+}_{Al}-doped pyrope > Ti^{3+}_{Al}-doped pyrope > geikielite ($MgTiO_3$) > $Mg_{0.5}Fe_{0.5}TiO_3$ > Ti^{3+}_{Mg}-doped clinopyroxene and orthopyroxene > ilmenite ($FeTiO_3$) > rutile.

Ti^{4+}_{Si}-doped olivine, clinopyroxene, orthopyroxene, and pyrope have similar 10^3lnβ, independent of the mineral species and their Ti^{4+} contents. Likewise, Ti^{3+}_{Mg}-doped clinopyroxene and orthopyroxene have similar 10^3lnβ values, which are insensitive to their Ti^{3+} contents. In contrast, in orthopyroxene, the 10^3lnβ of $^{44}Ca/^{40}Ca$ strongly depends on the Ca concentration in orthopyroxene within a narrow Ca concentration range but become insensitive to Ca concentration when it is lower

than a threshold value (Feng et al., 2014; Wang et al., 2017a). Similar effect is also found for $10^3\ln\beta$ of $^{26}Mg/^{24}Mg$ in carbonates (Wang et al., 2017b; Wang et al., 2019). Consequently, it can be inferred that the Ti content investigated in here should be lower than the threshold concentration, below which the $10^3\ln\beta$ of $^{49}Ti/^{47}Ti$ does not vary with the Ti content in silicate minerals (Fig. 2). However, the $10^3\ln\beta$ of $^{49}Ti/^{47}Ti$ of geikielite-ilmenite solutions significantly decrease with increasing Fe content, and the difference of $10^3\ln\beta$ between $MgTiO_3$ and $FeTiO_3$ is 0.25 ‰ at 1000 K. On the other hand, the $10^3\ln\beta$ of silicate minerals are also controlled by the sites occupied by Ti. For example, at 1000 K, the difference of $10^3\ln\beta$between Ti^{4+}_{Si}-doped and Ti^{4+}_{Al}-doped pyrope is 0.45 ‰, and that between Ti^{4+}_{Si}-doped and Ti^{3+}_{Mg}-doped clinopyroxene is ~ 0.87 ‰.

4. Discussion

4.1 Controlling factors on $10^3\ln\beta$ of $^{49}Ti/^{47}Ti$

At a given temperature and pressure, mass-dependent equilibrium isotope fractionation factors are dominantly controlled by the relative bond strengths (Bigeleisen and Mayer, 1947; Urey, 1947), which are jointly determined by various factors including bond length, CN, oxidation state, and electronic configuration. In general, shorter bonds are stronger with higher vibrational frequencies and enriched in heavier isotopes relative to longer and weaker bonds (Urey, 1947; Schauble et al., 2004; Hill and Schauble, 2008; Young et al., 2009;

Huang et al., 2013; Huang et al., 2014). For instance, our previous works (Feng et al., 2014; Wang et al., 2017a, b; Li et al., 2019) have demonstrated that the 10^3lnβ of $^{26}Mg/^{24}Mg$ for carbonates, the 10^3lnβ of $^{44}Ca/^{40}Ca$ for orthopyroxene, and the 10^3lnβ of $^{41}K/^{39}K$ for feldspars are negatively correlated with their average Mg-O, Ca-O, and K-O bond lengths, respectively.

Similarly, the 10^3lnβ of $^{49}Ti/^{47}Ti$ for all calculated silicate minerals show a general negative correlation with the average Ti-O bond lengths (Fig. 3a). Within geikielite-ilmenite solid solutions, the 10^3lnβ is also linearly correlated with the average Ti-O bond length. This is mainly because geikielite-ilmenite solid solutions have similar crystal structures, so that their 10^3lnβ are dominantly controlled by the average Ti-O bond lengths. Compared to Ti^{3+}_{Mg}-doped clinopyroxene and orthopyroxene, ilmenite and rutile have shorter average Ti-O bond lengths but smaller 10^3lnβ values (Fig. 2 and Fig. 3a), although Ti is all six-fold coordinated in those minerals (Table 1). These exceptions reveal that Ti-O bond length does not perfectly describe 10^3lnβ. Other parameters are also important, including the electronegativity of the second closest atoms relative to Ti atom (the closest atom is O), which probably affect the interaction between Ti atom and its surrounding atoms. Furthermore, the valence state of Ti could also influence the 10^3lnβ. Ti^{4+} and Ti^{3+} can occupy the octahedral Al site in pyrope through the $Al^{3+}+Si^{4+}\leftrightarrow Ti^{4+}+Al^{3+}$ and $Al^{3+}\leftrightarrow Ti^{3+}$ substitutions, respectively; hence the Ti^{4+} bonding environment in pyrope should be similar to that of Ti^{3+}. Nevertheless, the 10^3lnβ of Ti^{4+}_{Al}-doped pyrope is significantly

larger than of Ti^{3+}_{Al}-doped pyrope. This is mainly because the valence state of Ti in the octahedral Al site affects the average Ti-O bond length (Table 1 and Fig. 3a).

To quantify the dominant factor of $10^3 ln\beta$, the bond strength, we calculated the average force constant of Ti, $<F>$ (in N/m) (Table 2) using the partial phonon density of state *g(E)* of Ti following Dauphas et al. (2012):

$$< F >= \frac{M}{\hbar^2} \int_0^{+\infty} E^2 g(E) dE \quad (5)$$

where *M* is the mass of Ti, and $\hbar$ is the reduced Planck constant. As shown in Fig. 3b, at 1000 K $10^3 ln\beta$ are linearly, positively correlated with $<F>$ of Ti. The $<F>$ of Ti occupying the tetrahedral Si sites in silicate minerals have a small variation and are the largest among all calculated minerals, completely explaining the largest $10^3 ln\beta$ in those Ti^{4+}_{Si}-doped silicate minerals (Table 2 and Fig. 3b). Likewise, rutile has the smallest $<F>$ of Ti, and hence it has the smallest $10^3 ln\beta$. In particular, the $<F>$ of Ti in geikielite-ilmenite solid solutions linearly decreases with increasing Fe/(Fe+Mg) (Table 2), which explains the linear correlation between the $10^3 ln\beta$ and Fe/(Fe+Mg) in geikielite-ilmenite solid solutions. Therefore, the bond strength is better measured by the average force constant, which dominantly determines $10^3 ln\beta$.

4.2 Equilibrium inter-mineral Ti isotope fractionation factors

Because clinopyroxene is a common Ti-bearing mineral in silicate rocks, it is used as a reference to report equilibrium inter-mineral Ti isotope fractionation factors ($10^3 ln\alpha$ of $^{49}Ti/^{47}Ti$). The $10^3 ln\alpha$ between minerals and Ti^{4+}_{Si}-doped clinopyroxene as a function of temperature are plotted in Fig. 4, and their polynomial fitting factors are

403 reported in Table 3. The $10^3\ln\alpha$ between other silicate minerals (olivine,
404 orthopyroxene, and pyrope) and clinopyroxene are close to zero when Ti occupies the
405 tetrahedral Si sites. At 1000 K, the $10^3\ln\alpha_{\text{mineral-clinopyroxene}}$ only ranges from 0.077 ‰
406 for olivine to -0.049 ‰ for orthopyroxene regardless of their Ti concentrations (Table
407 3). In contrast, if Ti^{4+} occupies the octahedral Al site in pyrope through the
408 $Al^{3+}+Si^{4+}\leftrightarrow Ti^{4+}+Al^{3+}$ substitution, the $10^3\ln\alpha_{\text{pyrope-clinopyroxene}}$ will be around -0.5 ‰ at
409 1000 K (Table 3). As both $Al^{3+}+Si^{4+}\leftrightarrow Ti^{4+}+Al^{3+}$ and $Si^{4+}\leftrightarrow Ti^{4+}$ substitutions are
410 important for the incorporation of Ti^{4+} into pyrope from the perspective of total
411 energy, it is inferred that pyrope is relatively enriched in light Ti isotopes compared to
412 Ti^{4+}_{Si}-doped clinopyroxene. In addition, the $10^3\ln\alpha_{\text{mineral-clinopyroxene}}$ between
413 Ti^{3+}_{Mg}-doped clinopyroxene and orthopyroxene is up to ~ -0.9 ‰ at 1000 K (Table 3),
414 indicating the extremely enrichment of light Ti isotope in Ti^{3+}-bearing species relative
415 to the Ti^{4+}-bearing minerals. This inference may be important in assessing the Ti
416 isotope data in lunar rocks (Miller et al., 2016; Simon and Sutton, 2017).

417 **4.3 Implications for Ti isotope geochemistry**

418 Krawczynski et al. (2009) demonstrated that pyroxenes and garnets could
419 contain a certain percentage of Ti^{3+} under reducing condition (e.g., 2 log units below
420 the iron–w sti te buffer). In Apollo 14 aluminous basalts 14053 and 14072, 0–60% of
421 the Ti in pyroxene are trivalent (Simon and Sutton, 2017), although most pyroxenes
422 contain little or no detectable Ti^{3+}. The pyroxene with the most reduced Ti, i.e., lowest
423 $Ti^{4+}/(Ti^{4+} + Ti^{3+})$, was thought to crystallize before plagioclase, while the pyroxene

424 crystallizing from the melt after plagioclase came in dominantly contains Ti^{4+} (Simon
425 and Sutton, 2017). On the other hand, a recent experimental study conducted by
426 Leitzke et al. (2018) also suggested that Ti^{3+} only occurs in silicate minerals.
427 According to our results (Fig. 4), the Ti^{3+}-bearing lunar pyroxene should be enriched
428 light Ti isotopes relative to other Ti^{4+}-bearing pyroxenes, a prediction to be tested by
429 future study. Moreover, some pyroxenes in refractory inclusions in chondrites have a
430 $Ti^{3+}/(Ti^{3+}+Ti^{4+})$ ratio of ~ 0.4 (Simon et al., 2007), and some ordinary and enstatite
431 chondrites are also enriched in Ti^{3+} (Simon et al., 2016). Thus, due to the large $10^3 ln\alpha$
432 between Ti^{3+} and Ti^{4+} species, Ti isotopes could be fractionated by the change of
433 redox state during the thermal metamorphism processes on ordinary and enstatite
434 chondrite parental bodies. Hence, Ti isotope composition can trace the thermal
435 metamorphism process.

436 However, negligible Ti^{3+} has been detected in terrestrial samples that originate
437 from more oxidizing environment relative to the iron–w sti te buffer, suggesting that
438 the Ti^{3+} species have a negligible contribution to the Ti isotope variation in terrestrial
439 samples (Millet et al., 2016; Greber et al., 2017a, b; Deng et al., 2019). In contrast,
440 Fe-Ti oxides (such as ilmenite and magnetite) play a key role in Ti isotope systematics
441 during magma differentiation (Millet et al., 2016; Greber et al., 2017a, b; Deng et al.,
442 2019). They suggested that Fe-Ti oxides should be enriched in light Ti isotopes
443 relative to the melt, but different Ti isotopic fractionation factors between Fe-Ti
444 oxides and melt ($\Delta^{49}Ti^{oxides\text{-}melt}$) were inferred. In detail, Millet et al. (2016) found that

445 the $\Delta^{49}Ti^{oxides\text{-}melt} = -0.23\times10^6/T^2$ (T is temperature in Kelvin) based on the Agung
446 volcanic samples with a SiO_2 range of 54-65 wt.%. In contrast, based on Hekla lavas
447 with a wide SiO_2 range of 46.47-72.07 wt.%, Deng et al. (2019) proposed that the
448 $\Delta^{49}Ti^{oxides\text{-}melt}$ should be ~-0.1‰ at ~1500 K and ~-0.5‰ at ~1150 K, which
449 indicates that $\Delta^{49}Ti^{oxides\text{-}melt}$ is not only controlled by temperature. Deng et al.
450 (2019) speculated that the change of silicate melt structure with increasing SiO_2
451 contents causes the variation in $\Delta^{49}Ti^{oxides\text{-}melt}$ (Farges and Brown, 1997). Thus, the
452 temperature dependence of $\Delta^{49}Ti^{oxides\text{-}melt}$ in Millet et al. (2016) is only valid for melt
453 with low SiO_2 content. In fact, $\Delta^{49}Ti^{oxides\text{-}melt}$ is a function of both temperature and
454 melt SiO_2 content (Deng et al., 2019).

455 Our results show that the $10^3\ln\alpha$ between ilmenite and Ti^{4+}_{Si}-doped
456 clinopyroxene is up to -0.67‰ at 1200 K. Because estimating the $10^3\ln\beta$ of melts is
457 still a challenge, the $10^3\ln\alpha$ between ilmenite and silicate melt needs to be determined
458 in future study. As the local structure of Ti in silicate melt is different from the one in
459 Ti^{4+}_{Si}-doped clinopyroxene (Farges and Brown, 1997), Ti isotope fractionation
460 between the melt and Ti^{4+}_{Si}-doped silicate minerals could be significant, and the
461 $10^3\ln\alpha$ between ilmenite and Ti^{4+}_{Si}-doped clinopyroxene cannot be simply taken as
462 the one between ilmenite and silicate melt. However, our calculations show that the
463 $10^3\ln\alpha$ between geikielite-ilmenite solid solutions and Ti^{4+}_{Si}-doped clinopyroxene
464 significantly decreases with increasing Mg/(Fe+Mg) ratio in geikielite-ilmenite solid
465 solutions, with $10^3\ln\alpha_{MgTiO3\text{-}clinopyroxene}$ up to -0.49 ‰ at 1200 K (Table 3 and Fig. 4).

Thus, the $10^3\ln\alpha$ between ilmenite and melt is controlled by both the melt structure (SiO_2 content) and the composition of geikielite-ilmenite solid solutions. Additionally, Ti-magnetite, with a large variable composition range, also plays an important role controlling Ti isotope behaviors during magma differentiation, because it is a major Fe-Ti oxide during terrestrial basaltic magma evolution compared to ilmenite (e.g., Helz, 1987; Zhang et al., 2018). It is expected that the $10^3\ln\beta$ of magnetite is significantly affected by its Ti content, and hence the $10^3\ln\alpha$ between magnetite and silicate melt is also controlled by the Ti content in magnetite. As a consequence, the chemical composition of Fe-Ti oxides may significantly contribute to the Ti isotopic variability found in natural rocks (Millet et al., 2016; Greber et al., 2017a, b; Deng et al., 2019). Further studies on the $10^3\ln\beta$ of Ti-magnetite are required for a better understanding of the role of Fe-Ti oxides controlling the Ti isotope composition during magma evolution.

4.4 A potential Ti isotope thermometer

Temperature is an important parameter controlling magma evolution. Deng et al. (2019) estimated the temperatures during fractional crystallization of Fe-Ti oxides by calculating liquidus temperatures of the samples using rhyolite-melts with an assumed pressure and pre-eruptive H_2O/K_2O ratio. Our results demonstrate that the large $10^3\ln\alpha$ of $^{49}Ti/^{47}Ti$ between ilmenite and clinopyroxene can be used to evaluate whether the Ti isotope exchange in natural samples have reached the equilibrium state or not. The relationship between $10^3\ln\alpha_{ilmenite\text{-}clinopyroxene}$ and temperature can be further

used to independently determine the equilibrium temperature (Fig. 5). For example, the estimated $10^3\ln\alpha_{FeTiO3\text{-}clinopyroxene}$ ranging from -0.91 ‰ to -0.47 ‰ corresponds to temperature increasing from 1000 K to 1400 K. Since the $10^3\ln\alpha_{ilmenite\text{-}clinopyroxene}$ is not only controlled by temperature but also significantly depends on its Mg/(Fe+Mg) ratio, the determination of chemical composition of ilmenite is important for the accurate temperature estimation. Standard error of the estimation (SEE) of temperature can be estimated based on the combination of current analytical precision of Ti isotope composition (Millet and Dauphas, 2014) and the uncertainty of our calculated inter-mineral fractionation factor. Here we assumed that the analytical uncertainty for Ti isotope measurements of minerals is the same to the level of current analytical precision of Ti isotope composition (Millet and Dauphas, 2014). For instance, if the relationship between $10^3\ln\alpha_{FeTiO3\text{-}clinopyroxene}$ and temperature is adopted, the standard error at 1200 K is about 40 K, which is comparable to that of the elemental geothermometer (Putirka, 2008, 2016). Consequently, the inter-mineral Ti isotope fractionation between ilmenite and clinopyroxene could provide independent constraint on the equilibrium temperature.

5. Conclusions

This study presents the first investigation of equilibrium inter-mineral Ti isotope fractionation among a large number of silicate minerals and Fe-Ti oxides based on the DFT. Our results find large variation in $10^3\ln\beta$ of $^{49}Ti/^{47}Ti$. It decreases in the order of

508 Ti^{4+}_{Si}-doped olivine, clinopyroxene, orthopyroxene, and pyrope > Ti^{4+}_{Al}-doped
509 pyrope > Ti^{3+}_{Al}-doped pyrope > geikielite ($MgTiO_3$) > $Mg_{0.5}Fe_{0.5}TiO_3$ > Ti^{3+}_{Mg}-doped
510 clinopyroxene and orthopyroxene > ilmenite ($FeTiO_3$) > rutile. The $10^3 ln\beta$ of
511 Ti^{4+}_{Si}-doped and Ti^{3+}_{Mg}-doped silicate minerals are not sensitive to their Ti^{4+} and Ti^{3+}
512 contents, respectively. However, the $10^3 ln\beta$ of geikielite-ilmenite solutions
513 significantly decrease with increasing Fe/(Fe+Mg) ratio. Notably, the $10^3 ln\beta$ is
514 linearly, positively correlated to the Ti force constant, which is significantly affected
515 by the average Ti-O bond length and the valence state of Ti.

516 There is no significant Ti isotope fractionation among Ti^{4+}_{Si}-doped
517 clinopyroxene, orthopyroxene, olivine, and pyrope. However, redox condition plays
518 an important role fractionating Ti isotopes. Specifically, Ti^{3+}_{Mg}-doped clinopyroxene
519 and orthopyroxene are extremely enriched in light Ti isotopes relative to those
520 Ti^{4+}_{Si}-doped species. Consequently, Ti isotopes might be able to trace redox condition
521 under extremely reducing conditions, such as that during the lunar magma ocean
522 evolution and enstatite chondrite formation. In terrestrial samples, Fe-Ti oxides (such
523 as ilmenite) play a key role fractionating Ti isotopes during magma differentiation.
524 Our calculations demonstrate the enrichment of light Ti isotopes in ilmenite relative to
525 Ti^{4+}_{Si}-doped silicate minerals with $10^3 ln\alpha_{FeTiO3\text{-}clinopyroxene}$ of $^{49}Ti/^{47}Ti$ is up to -0.67‰
526 at 1200 K. In particular, the $10^3 ln\alpha$ between Fe-Ti oxides and melt also strongly
527 depends on the chemical composition of Fe-Ti oxides, which may significantly
528 contribute to the Ti isotopic variability during magma differentiation. In addition, the

529 inter-mineral Ti isotope fractionation between ilmenite and clinopyroxene can be used
530 as a thermometer, with the estimated temperature precision comparable to that of
531 elemental geothermometer if the analytical uncertainty for Ti isotope measurements
532 of minerals is the same to the level of current analytical precision of Ti isotope
533 composition.
534
535 **Acknowledgments**
536 This work is supported by the Strategic Priority Research Program (B) of the Chinese
537 Academy of Sciences (grant XDB18000000), Natural Science Foundation of China
538 (41590621, 41473011, 41721002), 111 Project and Special Program for Applied
539 Research on Super Computation of the NSFC-Guangdong Joint Fund. SH
540 acknowledges support from NSF EAR-1524387. Some computations were conducted
541 in the Supercomputing Center of the University of Science and Technology of China.

Tables

Table 1. Average Ti-O bond lengths, coordination numbers, and force constant of Ti in major silicate minerals, geikielite-ilmenite solid solutions, and rutile.

Minerals	Chemical composition	Ti content	Average Ti-O bond length (Å)	CN	Force constant (N/m)
clinopyroxene $Si^{4+}\leftrightarrow Ti^{4+}$	$Mg_8Ca_8Si_{15}TiO_{48}$	Ti/(Ti+Si)=1/16, 2c	1.8139	4	586.8
	$Mg_{16}Ca_{16}Si_{31}TiO_{96}$	Ti/(Ti+Si)=1/32, 2b, 2c	1.8126	4	596.2
	$Mg_{24}Ca_{24}Si_{47}TiO_{144}$	Ti/(Ti+Si)=1/48, 2b, 3c	1.8133	4	591.6
	$Mg_{32}Ca_{32}Si_{63}TiO_{192}$	Ti/(Ti+Si)=1/64, 2a, 2b, 2c	1.8127	4	591.8
clinopyroxene $Mg^{2+}+Si^{4+}\leftrightarrow Ti^{3+}+Al^{3+}$	$Mg_7TiCa_8Si_{15}AlO_{48}$	Ti/(Ti+Si)=1/16, 2c	2.0489	6	352.6
	$Mg_{15}TiCa_{16}Si_{31}AlO_{96}$	Ti/(Ti+Si)=1/32, 2b, 2c	2.0491	6	356.9
orthopyroxene $Si^{4+}\leftrightarrow Ti^{4+}$	$Mg_{16}Si_{15}TiO_{48}$	Ti/(Ti+Si)=1/16	1.8176	4	587.2
	$Mg_{32}Si_{31}TiO_{96}$	Ti/(Ti+Si)=1/32, 2c	1.8181	4	584.5
	$Mg_{48}Si_{47}TiO_{144}$	Ti/(Ti+Si)=1/48, 3c	1.8189	4	578.5
	$Mg_{64}Si_{63}TiO_{192}$	Ti/(Ti+Si)=1/64, 2b, 2c	1.8182	4	580.4
orthopyroxene $Mg^{2+}+Si^{4+}\leftrightarrow Ti^{3+}+Al^{3+}$	$Mg_{15}TiSi_{15}AlO_{48}$	Ti/(Ti+Si)=1/16	2.0438	6	354.3
	$Mg_{31}TiSi_{31}AlO_{96}$	Ti/(Ti+Si)=1/32, 2c	2.0448	6	352.7
olivine $Si^{4+}\leftrightarrow Ti^{4+}$	$Mg_{32}Si_{15}TiO_{64}$	Ti/(Ti+Si)=1/16, 2a, 2c	1.8100	4	604.4
	$Mg_{64}Si_{31}TiO_{128}$	Ti/(Ti+Si)=1/32, 2a, 2b, 2c	1.8095	4	611.2
pyrope $Al^{3+}+Si^{4+}\leftrightarrow Ti^{4+}+Al^{3+}$	$Mg_{12}Al_7TiSi_{11}AlO_{48}$	Ti/(Ti+Si+Al)=1/20[#]	1.9306	6	446.5
	$Mg_{24}Al_{15}TiSi_{23}AlO_{96}$	Ti/(Ti+Si+Al)=1/40[*]	1.9286	6	457.1
$Si^{4+}\leftrightarrow Ti^{4+}$	$Mg_{24}Al_{16}Si_{23}TiO_{96}$	Ti/(Ti+Si+Al)=1/40[*]	1.8083	4	578.6
$Al^{3+}\leftrightarrow Ti^{3+}$	$Mg_{24}Al_{15}TiSi_{24}O_{96}$	Ti/(Ti+Si+Al)=1/40[*]	1.9961	6	423.0
geikielite	$Mg_6Ti_6O_{18}$		1.9685	6	399.4
	$Mg_3Fe_3Ti_6O_{18}$		1.9717	6	370.0
ilmenite	$Fe_6Ti_6O_{18}$		1.9733	6	332.5
rutile	Ti_2O_4		1.9535	6	314.2

Abbreviations after Ti contents refer to the expansion way of primitive cells to generate supercells. For instance, "2a, 2b, 2c" represents the supercell is generated by expanding the primitive cell twice along a, b, and c directions. [#], the primitive cell of pyrope (80 atoms); [*], the conventional cell of pyrope (160 atoms)

549 **Table 2.** Polynomial fitting parameters of the reduced partition function ratios ($10^3 \ln\beta$)
550 of $^{49}Ti/^{47}Ti$ for Ti-doped silicate minerals, geikielite-ilmenite solid solutions, and
551 rutile.

clinopyroxene	chemical composition	Ti content	*a*	*b*	*c*
$Si^{4+} \leftrightarrow Ti^{4+}$	$Mg_8Ca_8Si_{15}TiO_{48}$	Ti/(Ti+Si)=1/16	2.23693	-4.097E-02	1.184E-03
	$Mg_{16}Ca_{16}Si_{31}TiO_{96}$	Ti/(Ti+Si)=1/32	2.27279	-4.163E-02	1.202E-03
	$Mg_{24}Ca_{24}Si_{47}TiO_{144}$	Ti/(Ti+Si)=1/48	2.25319	-4.127E-02	1.192E-03
	$Mg_{32}Ca_{32}Si_{63}TiO_{192}$	Ti/(Ti+Si)=1/64	2.25653	-4.133E-02	1.194E-03
$Mg^{2+}+Si^{4+} \leftrightarrow Ti^{3+}+Al^{3+}$	$Mg_7TiCa_8Si_{15}AlO_{48}$	Ti/(Ti+Si)=1/16	1.34285	-1.101E-02	1.906E-04
	$Mg_{15}TiCa_{16}Si_{31}AlO_{96}$	Ti/(Ti+Si)=1/32	1.36027	-1.115E-02	1.929E-04
orthopyroxene					
$Si^{4+} \leftrightarrow Ti^{4+}$	$Mg_{16}Si_{15}TiO_{48}$	Ti/(Ti+Si)=1/16	2.23666	-4.057E-02	1.166E-03
	$Mg_{32}Si_{31}TiO_{96}$	Ti/(Ti+Si)=1/32	2.22630	-4.038E-02	1.161E-03
	$Mg_{48}Si_{47}TiO_{144}$	Ti/(Ti+Si)=1/48	2.20346	-3.997E-02	1.149E-03
	$Mg_{64}Si_{63}TiO_{192}$	Ti/(Ti+Si)=1/64	2.21084	-4.010E-02	1.153E-03
$Mg^{2+}+Si^{4+} \leftrightarrow Ti^{3+}+Al^{3+}$	$Mg_{15}TiSi_{15}AlO_{48}$	Ti/(Ti+Si)=1/16	1.34287	-1.072E-02	1.775E-04
	$Mg_{31}TiSi_{31}AlO_{96}$	Ti/(Ti+Si)=1/32	1.33676	-1.067E-02	1.767E-04
olivine					
$Si^{4+} \leftrightarrow Ti^{4+}$	$Mg_{32}Si_{15}TiO_{64}$	Ti/(Ti+Si)=1/16	2.30449	-4.059E-02	1.080E-03
	$Mg_{64}Si_{31}TiO_{128}$	Ti/(Ti+Si)=1/32	2.33041	-4.105E-02	1.092E-03
pyrope					
$Al^{3+}+Si^{4+} \leftrightarrow Ti^{4+}+Al^{3+}$	$Mg_{12}Al_7TiSi_{11}AlO_{48}$	Ti/(Ti+Si+Al)=1/20	1.70195	-1.864E-02	3.799E-04
	$Mg_{24}Al_{15}TiSi_{23}AlO_{96}$	Ti/(Ti+Si+Al)=1/40	1.74244	-1.908E-02	3.889E-04
$Si^{4+} \leftrightarrow Ti^{4+}$	$Mg_{24}Al_{16}Si_{23}TiO_{96}$	Ti/(Ti+Si+Al)=1/40	2.20599	-4.040E-02	1.167E-03
$Al^{3+} \leftrightarrow Ti^{3+}$	$Mg_{24}Al_{15}TiSi_{24}O_{96}$	Ti/(Ti+Si+Al)=1/40	1.61237	-1.766E-02	3.600E-04
geikielite-ilmenite					
Geikielite	$Mg_6Ti_6O_{18}$		1.52316	-1.492E-02	2.649E-04
	$Mg_3Fe_3Ti_6O_{18}$		1.41088	-1.226E-02	1.937E-04
ilmenite	$Fe_6Ti_6O_{18}$		1.26749	-9.644E-03	1.352E-04
rutile	Ti_2O_4		1.19767	-9.585E-03	1.543E-04

552 Polynomial fitting equation is: $10^3 \ln\beta = ax + bx^2 + cx^3$, where $x = 10^6/T^2$. T is temperature

553 in Kelvin. Temperature range for polynomial fittings is from 673 K to 2500 K.

554 **Table 3.** Polynomial fitting parameters of the equilibrium Ti isotope fractionation
555 (10^3lnα of $^{49}Ti/^{47}Ti$) between other minerals and clinopyroxene with the chemical
556 composition of $Mg_{24}Ca_{24}Si_{47}TiO_{144}$. When Ti is incorporated into the clinopyroxene
557 through the $Si^{4+}\leftrightarrow Ti^{4+}$ substitution, Ti concentration in clinopyroxene does not show
558 significant effect on the 10^3lnα.

clinopyroxene	chemical composition	Ti content	*a*	*b*	*c*
$Mg^{2+}+Si^{4+}\leftrightarrow Ti^{3+}+Al^{3+}$	$Mg_7TiCa_8Si_{15}AlO_{48}$	Ti/(Ti+Si)=1/16	-0.91034	3.026E-02	-1.001E-03
	$Mg_{15}TiCa_{16}Si_{31}AlO_{96}$	Ti/(Ti+Si)=1/32	-0.89292	3.012E-02	-9.991E-04
orthopyroxene					
$Si^{4+}\leftrightarrow Ti^{4+}$	$Mg_{16}Si_{15}TiO_{48}$	Ti/(Ti+Si)=1/16	-0.01653	7.000E-05	-2.600E-05
	$Mg_{32}Si_{31}TiO_{96}$	Ti/(Ti+Si)=1/32	-0.02689	8.900E-04	-3.100E-05
	$Mg_{48}Si_{47}TiO_{144}$	Ti/(Ti+Si)=1/48	-0.04973	1.300E-03	-4.300E-05
	$Mg_{64}Si_{63}TiO_{192}$	Ti/(Ti+Si)=1/64	-0.04235	1.170E-03	-3.900E-05
$Mg^{2+}+Si^{4+}\leftrightarrow Ti^{3+}+Al^{3+}$	$Mg_{15}TiSi_{15}AlO_{48}$	Ti/(Ti+Si)=1/16	-0.91032	3.055E-02	-1.015E-03
	$Mg_{31}TiSi_{31}AlO_{96}$	Ti/(Ti+Si)=1/32	-0.91643	3.060E-02	-1.015E-03
olivine					
$Si^{4+}\leftrightarrow Ti^{4+}$	$Mg_{32}Si_{15}TiO_{64}$	Ti/(Ti+Si)=1/16	0.05130	6.800E-04	-1.120E-04
	$Mg_{64}Si_{31}TiO_{128}$	Ti/(Ti+Si)=1/32	0.07722	2.200E-04	-1.000E-04
pyrope					
$Al^{3+}+Si^{4+}\leftrightarrow Ti^{4+}+Al^{3+}$	$Mg_{12}Al_7TiSi_{11}AlO_{48}$	Ti/(Ti+Si+Al)=1/20	-0.55124	2.263E-02	-8.121E-04
	$Mg_{24}Al_{15}TiSi_{23}AlO_{96}$	Ti/(Ti+Si+Al)=1/40	-0.51075	2.219E-02	-8.031E-04
$Si^{4+}\leftrightarrow Ti^{4+}$	$Mg_{24}Al_{16}Si_{23}TiO_{96}$	Ti/(Ti+Si+Al)=1/40	-0.04720	8.700E-04	-2.500E-05
$Al^{3+}\leftrightarrow Ti^{3+}$	$Mg_{24}Al_{15}TiSi_{24}O_{96}$	Ti/(Ti+Si+Al)=1/40	-0.64082	2.361E-02	-8.320E-04
geikielite-ilmenite					
Geikielite	$Mg_6Ti_6O_{18}$		-0.73003	2.635E-02	-9.271E-04
	$Mg_3Fe_3Ti_6O_{18}$		-0.84231	2.901E-02	-9.983E-04
ilmenite	$Fe_6Ti_6O_{18}$		-0.98570	3.163E-02	-1.057E-03
rutile	Ti_2O_4		-1.05552	3.169E-02	-1.038E-03

559 Polynomial fitting equation is: $10^3\ln\alpha=ax+bx^2+cx^3$, where $x=10^6/T^2$. T is temperature
560 in Kelvin. Temperature range for polynomial fittings is from 673 K to 2500 K.

Figures

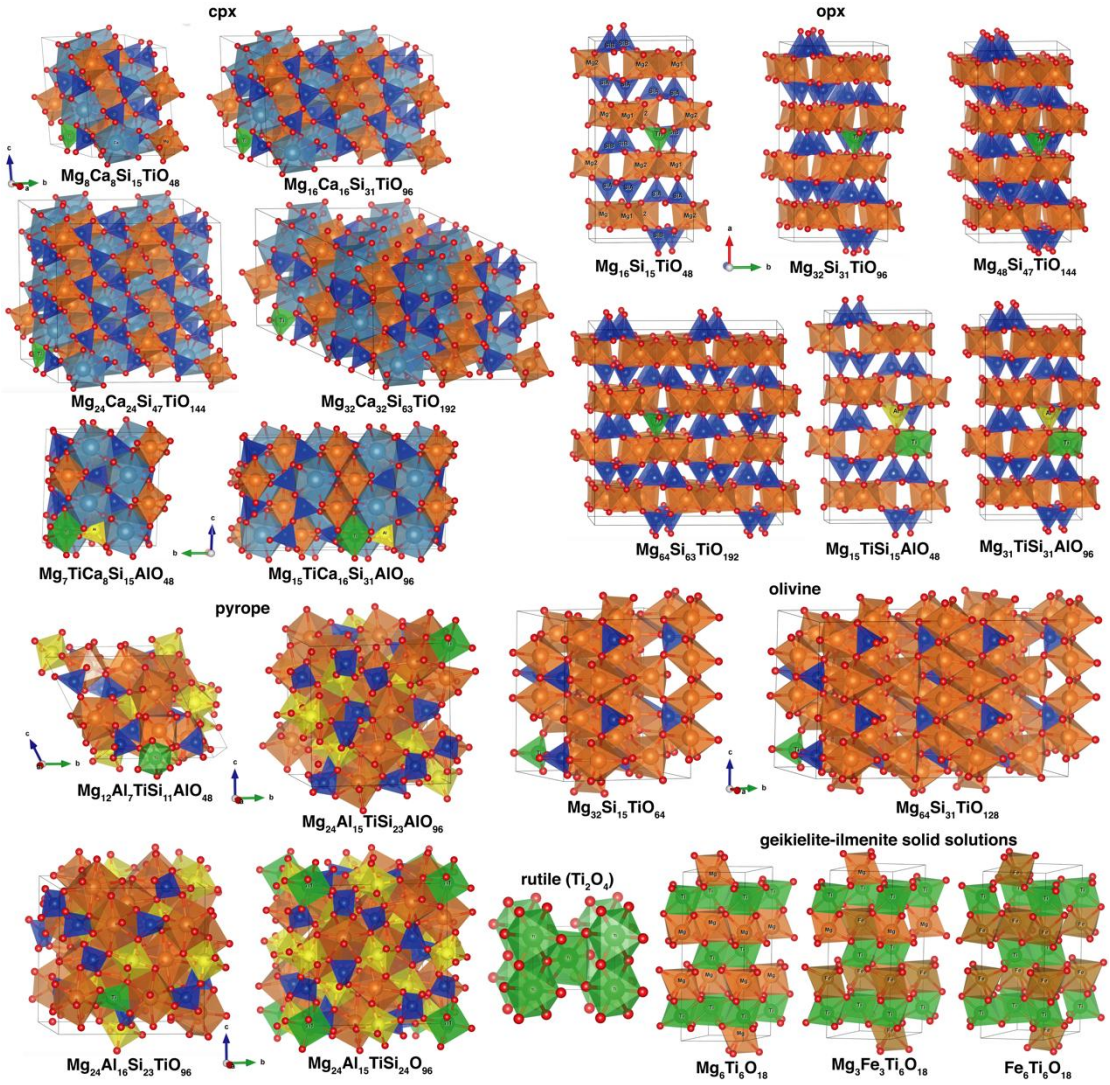

Figure 1. Relaxed crystal structures of Ti-doped clinopyroxene, orthopyroxene, olivine, pyrope, geikielite-ilmenite solid solutions ($MgTiO_3$, $Mg_{0.5}Fe_{0.5}TiO_3$, and $FeTiO_3$), and rutile (TiO_2). All crystal structures are drawn using the software "VESTA" (Momma and Izumi, 2008). Atomic colors: Ca, cyan; Mg, brown; Fe, dark brown; Si, blue; Ti, green; Al, yellow; O, red.

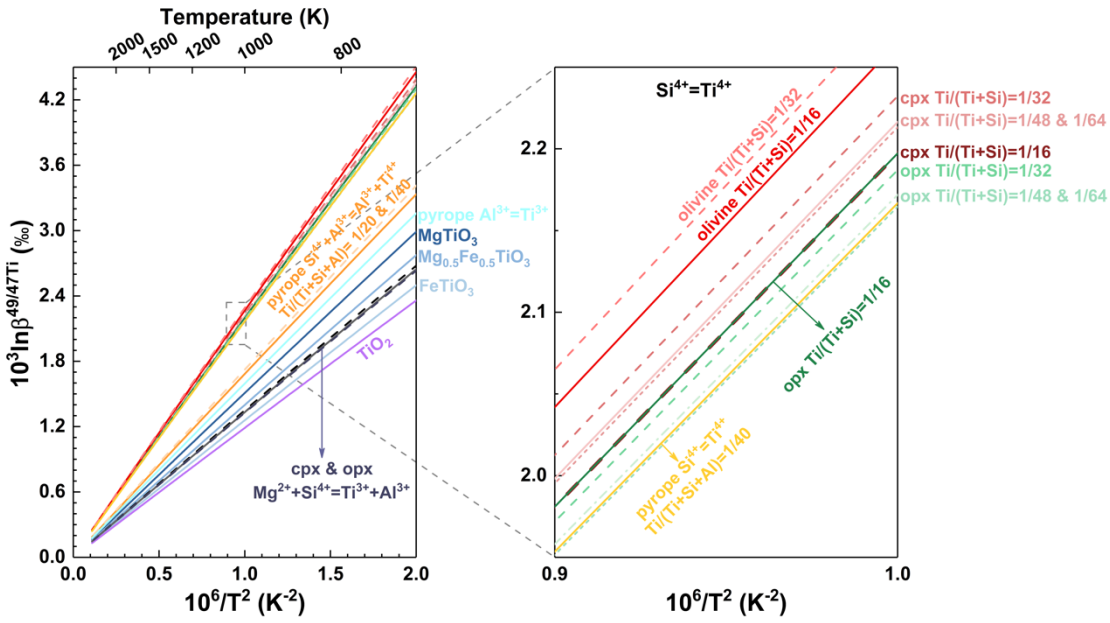

Figure 2. Temperature dependences of calculated reduced partition function ratios of $^{49}Ti/^{47}Ti$ ($10^3 ln\beta$) for clinopyroxene (cpx), orthopyroxene (cpx), olivine, pyrope, geikielite-ilmenite solid solutions ($MgTiO_3$, $Mg_{0.5}Fe_{0.5}TiO_3$, and $FeTiO_3$), and rutile (TiO_2).

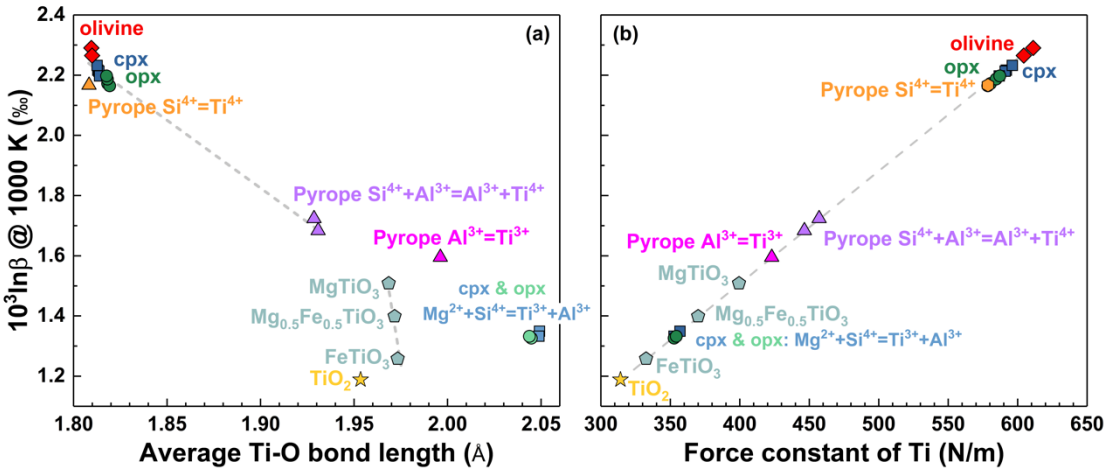

573

574 **Figure 3.** (a) The relationship between $10^3 \ln\beta$ $^{49}Ti/^{47}Ti$ at 1000 K and average Ti-O

575 bond length. (b) The linear correlation between $10^3 \ln\beta$ $^{49}Ti/^{47}Ti$ at 1000 K and force

576 constant of Ti in all calculated minerals. The coordination numbers (CN) of Ti in

577 clinopyroxene (cpx), olivine, and orthopyroxene (opx) are four, because one Ti atom

578 is incorporated into the Si tetrahedral site in these mineral structures. The CN of Ti in

579 pyrope depends on the substitution mechanism. Similarly, the CN of Ti is also four if

580 Ti is incorporated into the Si tetrahedral site in pyrope, and Ti atom is six-coordinated

581 when Ti atom occupies the Al octahedral site. The CNs of Ti in geikielite-ilmenite

582 solid solutions ($MgTiO_3$, $Mg_{0.5}Fe_{0.5}TiO_3$, and $FeTiO_3$) and rutile (TiO_2) are six.

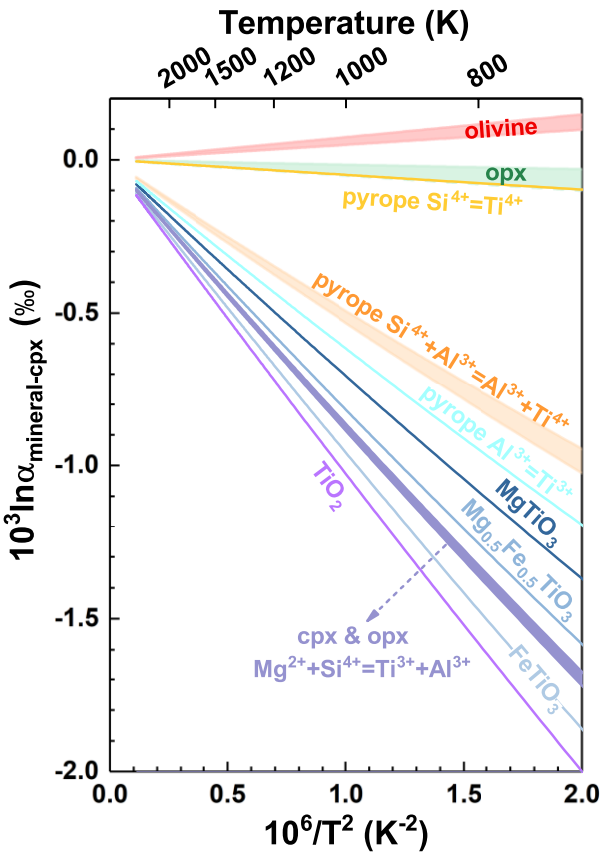

583

584 **Figure 4.** Equilibrium Ti isotope fractionation factors ($10^3\ln\alpha$) between other minerals

585 and clinopyroxene (cpx). The narrow red, green, and yellow regions represent

586 $10^3\ln\alpha_{\text{olivine-clinopyroxene}}$, $10^3\ln\alpha_{\text{orthopyroxene-clinopyroxene}}$, and $10^3\ln\alpha_{\text{pyrope-clinopyroxene}}$,

587 respectively.

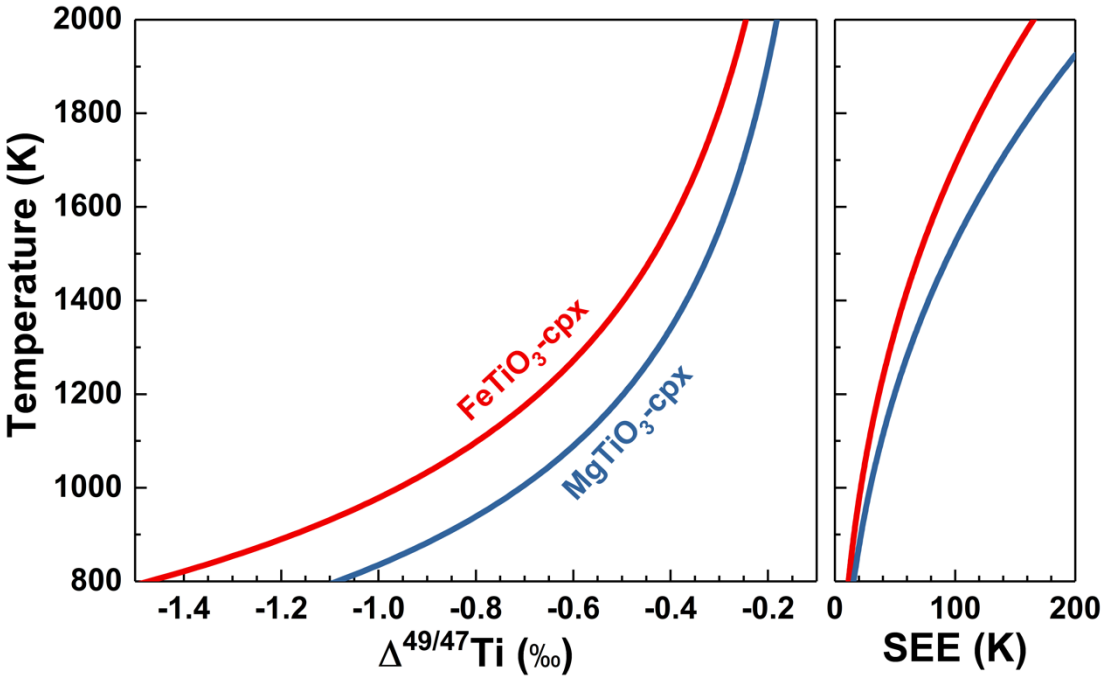

588

589 **Figure 5.** Relationship between temperature and $\Delta^{49/47}$Ti between (Fe, Mg)TiO_3 and

590 clinopyroxene as a potential Ti isotope thermometer. The Ti-doped clinopyroxene

591 structure that accommodates one Ti atom into the tetrahedral Si site through the

592 $Si^{4+}\leftrightarrow Ti^{4+}$ substitution is selected as the representative, because the Ti^{3+} content is

593 negligible in naturally occurring terrestrial samples (Millet et al., 2016). When Ti^{4+} is

594 incorporated into the clinopyroxene through the $Si^{4+}\leftrightarrow Ti^{4+}$ substitution, Ti

595 concentration in clinopyroxene does not show significant effect on its $10^3 ln\beta$ of

596 $^{49}Ti/^{47}Ti$. SEE refers to standard error of the estimation. Red and blue lines represent

597 ilmenite and geikielite, respectively.

References

Ackerson M. R., Watson E. B., Tailby N. D. and Spear F. S. (2017) Experimental investigation into the substitution mechanisms and solubility of Ti in garnet. *Am. Mineral.* **102**, 158–172.

Anders E. and Grevesse N. (1989) Abundances of the elements: Meteoritic and solar. *Geochim. Cosmochim. Acta* **53**, 197–214.

Anisimov V. I., Zaanen J. and Andersen O. K. (1991) Band theory and Mott insulators: Hubbard U instead of Stoner I. *Phys. Rev. B* **44**, 943–954.

Armbruster T. and Geiger C. A. (1993) Andradite crystal chemistry, dynamic X-site disorder and structural strain in silicate garnets. *Eur. J. Mineral.* **5**, 59–72.

Arroyo-De Dompablo M. E., Morales-Garca A. and Taravillo M. (2011) DFT+U calculations of crystal lattice, electronic structure, and phase stability under pressure of TiO_2 polymorphs. *J. Chem. Phys.* **135**.

Berry A. J., Walker A. M., Hermann J., O'Neill H. S. C., Foran G. J. and Gale J. D. (2007) Titanium substitution mechanisms in forsterite. *Chem. Geol.* **242**, 176–186.

Bigeleisen J. and Mayer M. G. (1947) Calculation of Equilibrium Constants for Isotopic Exchange Reactions. *J. Chem. Phys.* **15**, 261.

Cococcioni M. and de Gironcoli S. (2005) Linear response approach to the calculation of the effective interaction parameters in the LDA+U method. *Phys. Rev. B* **71**, 035105.

Curnan M. T. and Kitchin J. R. (2015) Investigating the Energetic Ordering of Stable and Metastable TiO_2 Polymorphs Using DFT+U and Hybrid Functionals. *J. Phys. Chem. C* **119**, 21060–21071.

Dauphas N., Roskosz M., Alp E. E., Golden D. C., Sio C. K., Tissot F. L. H., Hu M. Y., Zhao J., Gao L. and Morris R. V. (2012) A general moment NRIXS approach to the determination of equilibrium Fe isotopic fractionation factors: Application to goethite and jarosite. *Geochim. Cosmochim. Acta* **94**, 254–275.

Davis A. M., Zhang J., Greber N. D., Hu J., Tissot F. L. H. and Dauphas N. (2018) Titanium isotopes and rare earth patterns in CAIs: Evidence for thermal processing and gas-dust decoupling in the protoplanetary disk. *Geochim. Cosmochim. Acta* **221**, 275–295.

Deng Z., Chaussidon M., Savage P., Robert F., Pik R. and Moynier F. (2019) Titanium isotopes as a tracer for the plume or island arc affinity of felsic rocks. *Proc. Natl. Acad. Sci.*, 201809164.

Deng Z, Moynier F., Sossi P. A. and Chaussidon M. (2018) Bridging the depleted MORB mantle and the continental crust using titanium isotopes. *Geochemical Perspect. Lett.*, 11–15.

Deng Zhengbin, Moynier F., van Zuilen K., Sossi P. A., Pringle E. A. and Chaussidon M. (2018) Lack of resolvable titanium stable isotopic variations in bulk chondrites. *Geochim. Cosmochim. Acta* **239**, 409–419.

Farges F. and Brown G. E. (1997) Coordination chemistry of titanium (IV) in silicate

glasses and melts: IV. XANES studies of synthetic and natural volcanic glasses and tektites at ambient temperature and pressure. *Geochim. Cosmochim. Acta* **61**, 1863–1870.

Feng C., Qin T., Huang S., Wu Z. and Huang F. (2014) First-principles investigations of equilibrium calcium isotope fractionation between clinopyroxene and Ca-doped orthopyroxene. *Geochim. Cosmochim. Acta* **143**, 132–142.

Fujii T., Moynier F., Pons M.-L. and Albarède F. (2011) The origin of Zn isotope fractionation in sulfides. *Geochim. Cosmochim. Acta* **75**, 7632–7643.

Gao G. Y., Yao K. L. and Liu Z. L. (2006) First-principles study on magnetism and electronic structure of V-doped rutile TiO_2. *Phys. Lett. Sect. A Gen. At. Solid State Phys.* **359**, 523–527.

Gerke T. L., Kilinc A. I. and Sack R. O. (2005) Ti-content of high-Ca pyroxenes as a petrogenetic indicator: an experimental study of Mafic Alkaline Rocks from the Mt. Erebus volcanic region, Antarctica. *Contrib. to Mineral. Petrol.* **148**, 735–745.

Giannozzi P., Baroni S., Bonini N., Calandra M., Car R., Cavazzoni C., Ceresoli D., Chiarotti G. L., Cococcioni M., Dabo I., Dal Corso A., de Gironcoli S., Fabris S., Fratesi G., Gebauer R., Gerstmann U., Gougoussis C., Kokalj A., Lazzeri M., Martin-Samos L., Marzari N., Mauri F., Mazzarello R., Paolini S., Pasquarello A., Paulatto L., Sbraccia C., Scandolo S., Sclauzero G., Seitsonen A. P., Smogunov A., Umari P. and Wentzcovitch R. M. (2009) QUANTUM ESPRESSO: a modular and open-source software project for quantum simulations of materials. *J. Phys. Condens. Matter* **21**, 395502.

Greber Nicolas D., Dauphas N., Bekker A., Ptáček M. P., Bindeman I. N. and Hofmann A. (2017) Titanium isotopic evidence for felsic crust and plate tectonics 3.5 billion years ago. *Science* **357**, 1271–1274.

Greber Nicolas D, Dauphas N., Puchtel I. S., Hofmann B. A. and Arndt N. T. (2017) Titanium stable isotopic variations in chondrites, achondrites and lunar rocks. *Geochim. Cosmochim. Acta* **213**, 534–552.

Grew E. S., Locock A. J., Mills S. J., Galuskina I. O., Galuskin E. V. and Halenius U. (2013) Nomenclature of the garnet supergroup. *Am. Mineral.* **98**, 785–811.

Gwalani L. G., Rock N. M. S., Ramasamy R., Griffin B. J. and Mulai B. P. (2000) Complexly zoned Ti-rich melanite-schorlomite garnets from Ambadungar carbonatite-alkalic complex, Deccan Igneous Province, Gujarat State, Western India. *J. Asian Earth Sci.* **18**, 163–176.

Hermann J., O'Neill H. S. C. and Berry A. J. (2005) Titanium solubility in olivine in the system TiO_2–MgO–SiO_2: no evidence for an ultra-deep origin of Ti-bearing olivine. *Contrib. to Mineral. Petrol.* **148**, 746–760.

Hill P. S. and Schauble E. A. (2008) Modeling the effects of bond environment on equilibrium iron isotope fractionation in ferric aquo-chloro complexes. *Geochim. Cosmochim. Acta* **72**, 1939–1958.

Huang F., Chen L., Wu Z. and Wang W. (2013) First-principles calculations of

equilibrium Mg isotope fractionations between garnet, clinopyroxene, orthopyroxene, and olivine: Implications for Mg isotope thermometry. *Earth Planet. Sci. Lett.* **367**, 61–70.

Huang F., Wu Z., Huang S. and Wu F. (2014) First-principles calculations of equilibrium silicon isotope fractionation among mantle minerals. *Geochim. Cosmochim. Acta* **140**, 509–520.

Huang F., Zhou C., Wang W., Kang J. and Wu Z. (2019) First-principles calculations of equilibrium Ca isotope fractionation: Implications for oldhamite formation and evolution of lunar magma ocean. *Earth Planet. Sci. Lett.* **510**, 153–160.

Kööp L., Davis A. M., Nakashima D., Park C., Krot A. N., Nagashima K., Tenner T. J., Heck P. R. and Kita N. T. (2016a) A link between oxygen, calcium and titanium isotopes in26Al-poor hibonite-rich CAIs from Murchison and implications for the heterogeneity of dust reservoirs in the solar nebula. *Geochim. Cosmochim. Acta* **189**, 70–95.

Kööp L., Nakashima D., Heck P. R., Kita N. T., Tenner T. J., Krot A. N., Nagashima K., Park C. and Davis A. M. (2016b) New constraints on the relationship between ^{26}Al and oxygen, calcium, and titanium isotopic variation in the early Solar System from a multielement isotopic study of spinel-hibonite inclusions. *Geochim. Cosmochim. Acta* **184**, 151–172.

Krawczynski M. J., Sutton S. R., Grove T. L. and Newville M. (2009) Titanium oxidation state and coordination in the lunar high-Ti glass source mantle. The 40th Lunar and Planetary Science Conference.

Leitzke F. P., Fonseca R. O. C., Göttlicher J., Steininger R., Jahn S., Prescher C. and Lagos M. (2018) Ti K-edge XANES study on the coordination number and oxidation state of Titanium in pyroxene, olivine, armalcolite, ilmenite, and silicate glass during mare basalt petrogenesis. *Contrib. to Mineral. Petrol.* **173**, 103.

Lejaeghere K., Bihlmayer G., Bjorkman T., Blaha P., Blugel S., Blum V., Caliste D., Castelli I. E., Clark S. J., Dal Corso A., de Gironcoli S., Deutsch T., Dewhurst J. K., Di Marco I., Draxl C., Du ak M., Eriksson O., Flores-Livas J. A., Garrity K. F., Genovese L., Giannozzi P., Giantomassi M., Goedecker S., Gonze X., Granas O., Gross E. K. U., Gulans A., Gygi F., Hamann D. R., Hasnip P. J., Holzwarth N. A. W., Iu an D., Jochym D. B., Jollet F., Jones D., Kresse G., Koepernik K., Kucukbenli E., Kvashnin Y. O., Locht I. L. M., Lubeck S., Marsman M., Marzari N., Nitzsche U., Nordstrom L., Ozaki T., Paulatto L., Pickard C. J., Poelmans W., Probert M. I. J., Refson K., Richter M., Rignanese G.-M., Saha S., Scheffler M., Schlipf M., Schwarz K., Sharma S., Tavazza F., Thunstrom P., Tkatchenko A., Torrent M., Vanderbilt D., van Setten M. J., Van Speybroeck V., Wills J. M., Yates J. R., Zhang G.-X. and Cottenier S. (2016) Reproducibility in density functional theory calculations of solids. *Science* **351**, aad3000–aad3000.

Leya I., Schönbächler M., Krähenbühl U. and Halliday A. N. (2009) New titanium isotope data for allende and efremovka CAIs. *Astrophys. J.* **702**, 1118–1126.

Leya I., Schönbächler M., Wiechert U., Krähenbühl U. and Halliday A. N. (2008) Titanium isotopes and the radial heterogeneity of the solar system. *Earth Planet. Sci. Lett.* **266**, 233–244.

Li X. and Liu Y. (2011) Equilibrium Se isotope fractionation parameters: A first-principles study. *Earth Planet. Sci. Lett.* **304**, 113–120.

Li Y., Wang W., Huang S., Wang K. and Wu Z. (2019) First-principles investigation of the concentration effect on equilibrium fractionation of K isotopes in feldspars. *Geochim. Cosmochim. Acta* **245**, 374–384.

Lodders K. (2003) Solar system abundances and condensation temperatures of the elements. *Sci. York* **591**, 1220–1247.

McDonough W. F. and Sun S. -s. (1995) The composition of the Earth. *Chem. Geol.* **120**, 223–253.

Méheut M., Lazzeri M., Balan E. and Mauri F. (2009) Structural control over equilibrium silicon and oxygen isotopic fractionation: A first-principles density-functional theory study. *Chem. Geol.* **258**, 28–37.

Millet M. A. and Dauphas N. (2014) Ultra-precise titanium stable isotope measurements by double-spike high resolution MC-ICP-MS. *J. Anal. At. Spectrom.* **29**, 1444–1458.

Millet M., Dauphas N., Greber N. D., Burton K. W., Dale C. W., Debret B., Macpherson C. G., Nowell G. M. and Williams H. M. (2016) Titanium stable isotope investigation of magmatic processes on the Earth and Moon. *Earth Planet. Sci. Lett.* **449**, 197–205.

Momma K. and Izumi F. (2008) VESTA : a three-dimensional visualization system for electronic and structural analysis. *J. Appl. Crystallogr.* **41**, 653–658.

Perdew J. P. and Zunger A. (1981) Self-interaction correction to density-functional approximations for many-electron systems. *Phys. Rev. B* **23**, 5048–5079.

Portillo-Vélez N. S., Olvera-Neria O., Hernández-Pérez I. and Rubio-Ponce A. (2013) Localized electronic states induced by oxygen vacancies on anatase TiO_2 (101) surface. *Surf. Sci.* **616**, 115–119.

Proyer A., Habler G., Abart R., Wirth R., Krenn K. and Hoinkes G. (2013) TiO_2 exsolution from garnet by open-system precipitation: evidence from crystallographic and shape preferred orientation of rutile inclusions. *Contrib. to Mineral. Petrol.* **166**, 211–234.

Putirka K. (2016) Amphibole thermometers and barometers for igneous systems and some implications for eruption mechanisms of felsic magmas at arc volcanoes. *Am. Mineral.* **101**, 841–858.

Putirka K. D. (2008) Thermometers and Barometers for Volcanic Systems. *Rev. Mineral. Geochemistry* **69**, 61–120.

Qian W., Wang W., Zou F. and Wu Z. (2018) Elasticity of Orthoenstatite at High Pressure and Temperature: Implications for the Origin of Low VP/VS Zones in the Mantle Wedge. *Geophys. Res. Lett.* **45**, 665–673.

Richet P., Bottinga Y. and Javoy M. (1977) A Review of Hydrogen, Carbon, Nitrogen,

766 Oxygen, Sulphur, and Chlorine Stable Isotope Fractionation Among Gaseous
767 Molecules. *Annu. Rev. Earth Planet. Sci.* **5**, 65–110.
768 Rustad J. R. and Yin Q.-Z. (2009) Iron isotope fractionation in the Earth's lower
769 mantle. *Nat. Geosci.* **2**, 514–518.
770 Samat M. H., Ali A. M. M., Taib M. F. M., Hassan O. H. and Yahya M. Z. A. (2016)
771 Hubbard U calculations on optical properties of 3d transition metal oxide TiO_2.
772 *Results Phys.* **6**, 891–896.
773 Schauble E. A. (2011) First-principles estimates of equilibrium magnesium isotope
774 fractionation in silicate, oxide, carbonate and hexaaquamagnesium(2+) crystals.
775 *Geochim. Cosmochim. Acta* **75**, 844–869.
776 Schauble E., Rossman G. R. and Taylor H. P. (2004) Theoretical estimates of
777 equilibrium chromium-isotope fractionations. *Chem. Geol.* **205**, 99–114.
778 Simon J. I., Jordan M. K., Tappa M. J., Schauble E. A., Kohl I. E. and Young E. D.
779 (2017) Calcium and titanium isotope fractionation in refractory inclusions:
780 Tracers of condensation and inheritance in the early solar protoplanetary disk.
781 *Earth Planet. Sci. Lett.* **472**, 277–288.
782 Simon S. B. and Sutton S. R. (2017) Valence of Ti, V, and Cr in Apollo 14 aluminous
783 basalts 14053 and 14072. *Meteorit. Planet. Sci.* **52**, 2051–2066.
784 Simon S. B., Sutton S. R. and Grossman L. (2016) The valence and coordination of
785 titanium in ordinary and enstatite chondrites. *Geochim. Cosmochim. Acta* **189**,
786 377–390.
787 Simon S. B., Sutton S. R. and Grossman L. (2007) Valence of titanium and vanadium
788 in pyroxene in refractory inclusion interiors and rims. *Geochim. Cosmochim.*
789 *Acta* **71**, 3098–3118.
790 Skogby H., Halenius U., Kristiansson P. and Ohashi H. (2006) Titanium incorporation
791 and $VITi^{3+}$ -$IVTi^{4+}$ charge transfer in synthetic diopside. *Am. Mineral.* **91**,
792 1794–1801.
793 Togo A. and Tanaka I. (2015) First principles phonon calculations in materials
794 science. *Scr. Mater.* **108**, 1–5.
795 Trinquier A., Elliott T., Ulfbeck D., Coath C., Krot A. N. and Bizzarro M. (2009)
796 Origin of Nucleosynthetic Solar Protoplanetary Disk. *Science* **374**, 374–377.
797 Urey H. C. (1947) The thermodynamic properties of isotopic substances ed. S.-I.
798 Karato. *J. Chem. Soc.*, 562.
799 Vanderbilt D. (1990) Soft self-consistent pseudopotentials in a generalized eigenvalue
800 formalism. *Phys. Rev. B* **41**, 7892–7895.
801 Wang W., Qin T., Zhou C., Huang S., Wu Z. and Huang F. (2017a) Concentration
802 effect on equilibrium fractionation of Mg-Ca isotopes in carbonate minerals:
803 Insights from first-principles calculations. *Geochim. Cosmochim. Acta* **208**,
804 185–197.
805 Wang W. and Wu Z. (2018) Elasticity of Corundum at High Pressures and
806 Temperatures: Implications for Pyrope Decomposition and Al-Content Effect on
807 Elastic Properties of Bridgmanite. *J. Geophys. Res. Solid Earth* **123**, 1201–1216.

Wang W., Zhou C., Liu Y., Wu Z. and Huang F. (2019) Equilibrium Mg isotope fractionation among aqueous Mg^{2+}, carbonates, brucite and lizardite: Insights from first-principles molecular dynamics simulations. *Geochim. Cosmochim. Acta* **250**, 117–129.

Wang W., Zhou C., Qin T., Kang J., Huang S., Wu Z. and Huang F. (2017b) Effect of Ca content on equilibrium Ca isotope fractionation between orthopyroxene and clinopyroxene. *Geochim. Cosmochim. Acta* **219**, 44–56.

Wark D. A. and Watson E. B. (2006) TitaniQ: a titanium-in-quartz geothermometer. *Contrib. to Mineral. Petrol.* **152**, 743–754.

Watson E. B., Wark D. A. and Thomas J. B. (2006) Crystallization thermometers for zircon and rutile. *Contrib. to Mineral. Petrol.* **151**, 413–433.

Wentzcovitch R. M. (1991) Invariant molecular-dynamics approach to structural phase transitions. *Phys. Rev. B* **44**, 2358–2361.

Williams C. D., Janney P. E., Hines R. R. and Wadhwa M. (2016) Precise titanium isotope compositions of refractory inclusions in the Allende CV3 chondrite by LA-MC-ICPMS. *Chem. Geol.* **436**, 1–10.

Wu Z., Huang F. and Huang S. (2015) Isotope fractionation induced by phase transformation: First-principles investigation for Mg_2SiO_4. *Earth Planet. Sci. Lett.* **409**, 339–347.

Young E. D., Tonui E., Manning C. E., Schauble E. and Macris C. A. (2009) Spinel–olivine magnesium isotope thermometry in the mantle and implications for the Mg isotopic composition of Earth. *Earth Planet. Sci. Lett.* **288**, 524–533.

Zhang J., Dauphas N., Davis A. M., Leya I. and Fedkin A. (2012) The proto-Earth as a significant source of lunar material. *Nat. Geosci.* **5**, 251–255.

Zhang J., Dauphas N., Davis A. M. and Pourmand A. (2011) A new method for MC-ICPMS measurement of titanium isotopic composition: Identification of correlated isotope anomalies in meteorites. *J. Anal. At. Spectrom.* **26**, 2197–2205.

Zhang J., Huang S., Davis A. M., Dauphas N., Hashimoto A. and Jacobsen S. B. (2014) Calcium and titanium isotopic fractionations during evaporation. *Geochim. Cosmochim. Acta* **140**, 365–380.

Equilibrium inter-mineral titanium isotope fractionation: Implication for high-temperature titanium isotope geochemistry

Wenzhong Wang[a,*], Shichun Huang[b], Fang Huang[c], Xinmiao Zhao[d], Zhongqing Wu[a,*]

[a] Laboratory of Seismology and Physics of Earth's Interior, School of Earth and Space Sciences, University of Science and Technology of China, Hefei, Anhui 230026, China

[b] Department of Geoscience, University of Nevada, Las Vegas, NV 89154, United States

[c] CAS Key Laboratory of Crust-Mantle Materials and Environments, School of Earth and Space Sciences, University of Science and Technology of China, Hefei, Anhui 230026, China

[d] State Key Laboratory of Lithospheric Evolution, Institute of Geology and Geophysics, Chinese Academy of Sciences, Beijing 100029, China

5696 words, 5 figures, 3 tables, and supplementary materials

[*] Correspondences and requests for materials should be addressed to Wenzhong Wang (wz30304@mail.ustc.edu.cn) or Zhongqing Wu (wuzq10@ustc.edu.cn)

Abstract

Equilibrium Ti isotope fractionation factors among major Ti-bearing minerals are critical for understanding Ti isotope fractionation during magmatic processes. We use the first-principles calculations based on the density functional theory (DFT) to obtain Ti isotope reduced partition function ratios ($10^3\ln\beta$ of $^{49}Ti/^{47}Ti$) in a series of important Ti bearing minerals, including Ti-doped clinopyroxene, orthopyroxene, olivine, and pyrope, geikielite-ilmenite solid solutions, and rutile. There is a large variation in our calculated $10^3\ln\beta$, which are linearly correlated to their Ti force constants, a parameter related to the average Ti-O bond length and the Ti valence state. Among all studied minerals, silicates with Ti^{4+} occupying the tetrahedral Si site have the highest $10^3\ln\beta$, and rutile has the lowest $10^3\ln\beta$. The valence state also significantly controls the $10^3\ln\beta$. Typically, Ti^{3+}-doped silicates have lower $10^3\ln\beta$ than those of Ti^{4+}-doped silicates. At the natural abundance levels, the $10^3\ln\beta$ of Ti^{4+}_{Si}-doped and Ti^{3+}_{Mg}-doped (Ti^{3+} occupying the Mg site) silicate minerals show no concentration effect. That is, their $10^3\ln\beta$ do not vary with their Ti^{4+} and Ti^{3+} contents, respectively. In contrast, the $10^3\ln\beta$ of geikielite-ilmenite solutions significantly decrease with increasing Fe/(Fe+Mg) ratio.

Our calculations predict no significant Ti isotope fractionation among Ti^{4+}_{Si}-doped clinopyroxene, orthopyroxene, olivine, and pyrope (< 0.08 % at 1200 K), whereas the $10^3\ln\alpha$ between geikielite-ilmenite solutions and Ti^{4+}_{Si}-doped clinopyroxene ranges from ~-0.67‰ to -0.49‰ at 1200 K, supporting the hypothesis

that Fe-Ti oxides are important fractionating Ti isotopes during magma differentiation. Finally, the large equilibrium Ti isotope fractionation between geikielite-ilmenite solutions and clinopyroxene suggests that Ti isotopes can be used as a thermometer with precision comparable to that of elemental geothermometer.

Keywords: Ti isotopes; First-principle calculations; Fe-Ti oxides; silicate minerals; Equilibrium fractionation factors; Magma differentiation.

1. Introduction

Titanium (Ti) is an important rock-forming element in terrestrial planets (Anders and Grevesse, 1989; McDonough and Sun, 1995). It is lithophile, incompatible, and fluid-immobile, and it has been extensively used in high-temperature geochemistry. For example, the temperature dependent Ti solubility in quartz and zircon have been widely used as geothermometers (e.g., Watson et al., 2006; Wark and Watson, 2006). Titanium is also a highly refractory element (Lodders, 2003), playing an important role in our understanding of refractory inclusions in chondrites (e.g., Simon et al., 2007; Simon et al., 2017; Davis et al., 2018). In terrestrial rocks, Ti is usually present as Ti^{4+}. Significant amounts of Ti^{3+} could be present under extremely reduced conditions such as in lunar rocks and refractory inclusions (Simon et al., 2007; Simon and Sutton, 2017), and thus the Ti^{3+}/Ti^{4+} ratio can be used for measuring oxygen fugacity (e.g., Simon et al., 2007).

Titanium has five stable isotopes, ranging from ^{46}Ti (8.25%) to ^{50}Ti (5.18%). With the advancement in analytical techniques, Ti isotope composition has become an important cosmochemical and geochemical tracer (e.g., Leya et al., 2008, 2009; Trinquier et al., 2009; Zhang et al., 2011, 2012, 2014; Millet and Dauphas, 2014; Kööp et al., 2016a, b; Williams et al., 2016; Greber et al., 2017a, b; Simon et al., 2017; Davis et al., 2018; Deng et al., 2018a, b, 2019). For example, both mass-dependent and mass-independent Ti isotope variations have been reported in meteorites and their components, which are used to constrain the origin and evolution of early solar

system (Simon et al., 2017; Greber et al., 2017a; Davis et al., 2018; Deng et al., 2018a).

Titanium isotope composition can be also used to trace magma differentiation processes. Large mass-dependent Ti isotope variation, $\delta^{49}Ti$ ranging from −0.01 ± 0.03‰ to +2.01 ± 0.01‰ ($\delta^{49}Ti = [(^{49}Ti/^{47}Ti)_{sample} / (^{49}Ti/^{47}Ti)_{standard} - 1]*1000$ ‰), is observed in terrestrial rocks (Millet et al., 2016; Greber et al., 2017b; Deng et al., 2018b, 2019), which is thought to reflect Fe-Ti oxides fractionation during magma evolution. Specifically, Millet et al. (2016) found that $\delta^{49}Ti$ is positively correlated with SiO_2 content in differentiated terrestrial rocks, inferring that Fe-Ti oxides are enriched in light Ti isotopes relative to the melt. Using additional data from plume-related volcanoes (Hekla from Iceland, and Afar), Deng et al. (2019) identified two $\delta^{49}Ti$ vs. SiO_2 content trends, one defined by plume lavas and another by arc settings lavas. They argued that this is because the high Ti melt contents in plume lavas due to both high initial TiO_2 contents and delayed onset of Fe-Ti oxides from low oxygen fugacity drive the larger Ti isotope fractionation seen in plume lavas relative to arc setting lavas. Best fit for the relationship between $\delta^{49}Ti$ and f_{Ti}, the Ti proportion remaining in the melt, indicates that Ti isotope behaviors are controlled by the fractional crystallization of Ti-Fe oxides (such as ilmenite and titanomagnetite). In addition, Millet et al. (2016) also found that high-Ti lunar basalts have relatively higher $\delta^{49}Ti$ values than low-Ti mare basalts, which was ascribed to the Ti isotope fractionation induced by ilmenite (Millet et al., 2016). In igneous rocks, Fe-Ti oxides

88 are major hosts of Ti, which can be also incorporated into silicate minerals as a minor
89 element. The equilibrium Ti isotope fractionation factors among major Ti-oxides and
90 silicate minerals are important in understanding the reported δ^{49}Ti variations in both
91 terrestrial and lunar rocks. However, such data do not exist in the literature.

92 Due to the difficulty and uncertainty to reach the isotope exchange equilibrium
93 among minerals inside experiment charges, experimental determinations of
94 inter-mineral equilibrium isotope fractionation at high temperature are still
95 challenging. First-principles calculations based on the density functional theory (DFT)
96 predict inter-mineral isotope fractionation factors with accuracy and precision
97 comparable to some of the well-designed experiments (Lejaeghere et al., 2016). This
98 technique has been widely used to calculate equilibrium isotope fractionation in many
99 systems (e.g., Méheut et al., 2009; Rustad and Yin, 2009; Schauble, 2011; Li and Liu,
100 2011; Fujii et al., 2011; Huang et al., 2013; Feng et al., 2014; Wang, et al., 2017a, b;
101 Liu et al., 2018; Huang et al., 2019; Li et al., 2019).

102 Here we investigated the equilibrium inter-mineral Ti isotope fractionation
103 factors among Ti-doped clinopyroxene (clinopyroxene), orthopyroxene
104 (orthopyroxene), olivine, and pyrope, geikielite-ilmenite solid solutions, and rutile
105 using first-principles calculations based on the DFT. Ti is a minor element in silicate
106 minerals and the Ti contents in pyroxenes, olivine, and garnet vary significantly (e.g.,
107 Hermann et al., 2005; Gerke et al., 2005). Although Ti^{3+} does not occur in terrestrial
108 rocks, it is present in lunar rocks and refractory inclusions in chondrites (e.g., Simon

et al., 2007; Simon and Sutton, 2017), which were produced under extremely reducing conditions. Thus, both Ti^{4+}-doped and Ti^{3+}-doped silicate minerals are considered in this work. More importantly, because of mineral concentration effect on the equilibrium isotope fractionation (Feng et al., 2014; Wang et al., 2017a, b; Li et al., 2019), we also investigated the effect of silicate mineral Ti concentration on the equilibrium inter-mineral Ti isotope fractionation factors. This study for the first time provides fundamental equilibrium inter-mineral fractionation data to understand the Ti isotope behaviors during magmatic and metamorphic processes.

2. Calculation methods

2.1 Equilibrium isotope fractionation factor

According to Urey (1947), the isotopic substitution of a specific element in two phases would induce a difference in vibrational frequency properties, which results in mass-dependent equilibrium isotope fractionation between these two phases. Following Richet et al. (1977), the reduced partition function ratio β_A of the element X in phase A is the X isotope fractionation factor between the phase A and an ideal atomic gas. Based on the harmonic approximation, β_A can be written as:

$$\beta_A = \frac{Q_h}{Q_l} = \prod_i^{3N} \frac{u_{ih}}{u_{il}} \frac{e^{-\frac{1}{2}u_{ih}}}{1-e^{-u_{ih}}} \frac{1-e^{-u_{il}}}{e^{-\frac{1}{2}u_{il}}} \quad (1)$$

where *h* and *l* refer to the heavy and light isotopes, respectively, running index *i* refers to the i^{th} vibrational frequency, and *N* is the number of atoms in the unit cell. A phase with *N* atoms has *3N* vibrational modes and thus the product runs over all *3N* phonon

modes. Q_h and Q_l represent the vibrational partition function for the heavy and light isotopes, respectively. u_{ih} and u_{il} are defined as:

$$u_{ih\ or\ il} = \hbar\omega_{ih\ or\ il}/k_B T \quad (2)$$

where $\hbar$ and k_B are the Planck and Boltzmann constants, respectively, T is temperature in Kelvin, and $\omega_{ih\ or\ il}$ is the vibrational frequency of the i^{th} mode. Consequently, the equilibrium isotope fractionation factor between Phases A and B can be expressed as:

$$\Delta_{A-B} \approx 10^3 ln\alpha_{A-B} = 10^3 ln\beta_A - 10^3 ln\beta_B \quad (3)$$

2.2 First-principles calculations

We performed first-principles calculations using the software "Quantum Espresso" (Giannozzi et al., 2009), which is based on the DFT, plane wave, and pseudopotential, following a procedure similar to our previous studies (Huang et al., 2013; Feng et al., 2014; Wu et al., 2015; Wang et al., 2017a, b; Qian et al., 2018; Wang and Wu, 2018; Li et al., 2019). We adopted the local density approximation (LDA) (Perdew and Zunger, 1981) to describe the exchange correlation functional. The pseudopotentials of Mg, Ca, Si, Al, and O used in this study are the same as the ones used in our previous work (Huang et al., 2013; Feng et al., 2014; Wang et al., 2017b; Wang and Wu, 2018). The pseudopotentials of Ti and Fe were generated using the Vanderbilt method (Vanderbilt, 1990) with a valence configuration of $3s^2 3p^6 4s^2 3d^2$ and a cutoff radii of 1.8 Bohr for Ti, and $3s^2 3p^6 3d^{6.5} 4s^1 4p^0$ and 1.8 Bohr for Fe. In order to describe the large on-site Coulomb interactions among the localized electrons

151 (*3d* electrons of Fe and Ti) (Anisimov et al., 1991), we introduced a Hubbard U
152 correction to the LDA for all DFT calculations (LDA+U). Hubbard U values for Fe
153 and Ti atoms on different sites in all calculated minerals (Table S1) were
154 non-empirically determined using the linear response method (Cococcioni and de
155 Gironcoli, 2005).

156 We first optimized all crystal structures of Ti-bearing minerals using the variable
157 cell shape molecular dynamics method (Wentzcovitch, 1991) with different k-point
158 grids according to their unit cell sizes (see Table S1). The energy cutoff for plane
159 wave and charge density are set to 70 Ry and 700 Ry, respectively. The residual forces
160 converge within 10^{-4} Ry/Bohr. After the relaxed structures were obtained, we then
161 calculated phonon vibrational frequencies using the finite displacement method as
162 implemented in the open-source code PHONOPY (Togo and Tanaka, 2015). To make
163 comparisons of compare transverse-optical and longitudinal-optical frequencies of
164 rutile between theoretical predictions and experimental measurements, we also
165 calculated its vibrational frequencies based on the density-functional perturbation
166 theory (DFPT), which includes the effects of dielectric tensors and effective charges.
167 Hereafter all phonon calculations are based on the finite displacement method unless
168 specially mentioned. The reduced partition function ratios β of $^{49}Ti/^{47}Ti$ for all
169 calculated minerals can be obtained using Eq. (1). The finite displacement method and
170 DFPT give the similar β factor of rutile.

171 Some previous studies also performed DFT+U calculations to predict the

electronic structure and optical properties of TiO_2 polymorphs. For example, Gao et al. (2006) suggested that V-doped rutile TiO_2 is a half-metal within LDA while a semiconductor within the LDA+U. The DFT + U method has been also applied in Ti 3d of TiO_2 by Arroyo-De Dompablo et al. (2011) to improve the accuracy of standard DFT. Portillo-Vélez et al. (2013) also investigated the influence of surface oxygen vacancies in the structural and electronic properties of anatase TiO_2 (1 0 1) surface using Hubbard U correction. Curnan and Kitchin (2015) also performed a DFT+U study about the relative energetic ordering of rutile, anatase, brookite and columbite TiO_2 polymorphs. A recent study reported by Samat et al. (2016) also investigated the optical properties of titanium dioxide (TiO_2) in rutile, anatase and brookite phases via DFT+U calculations.

In order to check the effect of Hubbard U correction, we also performed LDA calculations for rutile, geikielite, clinopyroxene ($Mg_8Ca_8Si_{15}TiO_{48}$), and orthopyroxene ($Mg_{16}Si_{15}TiO_{48}$). The LDA results are compared to LDA+U results in Table S6-S7 and Figure S1-S2. The LDA predicts smaller static volumes and shorter average Ti-O bond lengths than LDA+U (Table S6). Both LDA and LDA+U underestimate mineral volumes at static conditions, but the ones calculated within LDA+U are closer to experimental values. When we considered the effects of zero-point motion and room temperature on volumes, the equation of states of rutile and geikielite calculated within LDA+U show great agreements with experimental measurements at 300 K (Fig. S3 and S4), revealing the validity of +U correction.

193 Unexpectedly, we find that LDA gives some negative frequencies for rutile (Fig. S1),
194 while LDA+U calculations predict normal phonon frequencies that are generally in
195 agreements with experimental measurements (Table S5). Thus, we cannot obtain the
196 $10^3 \ln\beta$ of rutile and its volume-pressure relationship from LDA calculations. For
197 clinopyroxene ($Mg_8Ca_8Si_{15}TiO_{48}$), and orthopyroxene ($Mg_{16}Si_{15}TiO_{48}$), LDA gives
198 larger $10^3 \ln\beta$ values than LDA+U (Table S6 and S7) because LDA predicts shorter
199 average Ti-O bond lengths than LDA+U (Table S6). However, the $10^3 \ln\alpha$ between
200 clinopyroxene and orthopyroxene from LDA calculations are similar to the one from
201 LDA+U calculations (0.02 ‰ for LDA+U vs. 0.03 ‰ for LDA at 1000 K). For
202 geikielite, +U correction shows a mild effect on vibrational frequencies (Fig. S2), and
203 the average Ti-O bond length and $10^3 \ln\beta$ calculated within LDA are only slightly
204 shorter and larger than those predicted by LDA+U (Table S6), respectively. Therefore,
205 we focus on the results calculated within LDA+U thereafter.
206
207 **3. Results**
208 **3.1 Ti incorporation into major silicate minerals**
209 Ti is a minor element in the major silicate minerals, such as olivine,
210 clinopyroxene, orthopyroxene, and garnet. The amount of TiO_2 in olivine is usually
211 lower than 1.0 wt% (Hermann et al., 2005), while pyroxenes and garnet can dissolve
212 up to several weight percent of TiO_2 (Gerke et al., 2005). Although major element
213 sites in these silicate minerals are well known, potential Ti substitution mechanisms

214 are pretty complicated and some are still under debate. In Ti-doped olivine, Ti is
215 negatively correlated with Si, but there is no correlation between Ti and Mg contents
216 (Hermann et al., 2005). This implies that Ti mainly substitutes for Si in the olivine
217 tetrahedral sites (Hermann et al., 2005; Berry et al., 2007). Simon et al. (2007; 2016)
218 reported both Ti^{3+} and Ti^{4+} in lunar pyroxenes, with Ti^{4+} preferentially occupying the
219 tetrahedral Si site and Ti^{3+} occupying the octahedral Mg position (M1) (Skogby et al.,
220 2006). Notably, Ti^{3+} only appears in some lunar pyroxenes produced under extremely
221 reducing conditions (Simon and Sutton, 2017), whereas there is no measurable Ti^{3+} in
222 terrestrial rocks. Garnet has a generalized chemical formula of $X^{2+}{}_3Y^{3+}{}_2Z^{4+}{}_3O_{12}$,
223 where X^{2+}, Y^{3+}, and Z^{4+} occupy the dodecahedral, octahedral, and tetrahedral sites,
224 respectively. In the upper mantle, garnet is mainly made of its Mg-Al end-member
225 pyrope ($Mg_3Al_2Si_3O_{12}$). Several substitution mechanisms have been proposed to
226 incorporate Ti into garnet, which can be divided into two types of site occupancies
227 (Ackerson et al., 2017). In one type, Ti^{4+} occupies the tetrahedral Z site through a
228 simple $Si^{4+}\leftrightarrow Ti^{4+}$ substitution (Armbruster and Geiger, 1993; Gwalani et al., 2000). In
229 the other type, Ti^{4+} occupies the octahedral Y site through a paired cation substitution,
230 such as $^{VI}Al^{3+}+{}^{IV}Si^{4+}\leftrightarrow{}^{VI}Ti^{4+}+{}^{IV}Al^{3+}$, to balance the charge (Grew et al., 2013; Proyer
231 et al., 2013; Ackerson et al., 2017). Under extremely reducing environment, Ti^{3+} can
232 be also directly incorporated into the octahedral Y site; however, terrestrial garnets
233 contains negligible amount of Ti^{3+} (Gwalani et al., 2000; Grew et al., 2013).
234 Consequently, Ti^{3+} is irrelevant to terrestrial rocks, and will not be further discussed in

235 the topic relevant to terrestrial rocks.

236 Here we investigated the configuration when Ti^{4+} occupies the tetrahedral Si site
237 in olivine, orthopyroxene, clinopyroxene, and pyrope through the $Si^{4+} \leftrightarrow Ti^{4+}$
238 substitution. Orthopyroxene has two nonequivalent tetrahedral Si sites, SiA and SiB.
239 Our calculations show that the energy difference between Ti^{4+} in the SiA and SiB sites
240 is large, 0.39 eV for orthopyroxene with Ti/(Ti+Si)=1/32, suggesting that Ti^{4+} prefers
241 the SiB site. Thus, orthopyroxene with Ti^{4+} occupying the SiB site was used in our
242 calculations. We also calculated the Ti-doped pyrope generated by coupled
243 substitution, $^{VI}Al^{3+}+^{IV}Si^{4+} \leftrightarrow ^{VI}Ti^{4+}+^{IV}Al^{3+}$. Particularly, Ti^{4+} occupies the octahedral
244 Al site, and the original Al^{3+} now occupies the nearest tetrahedral Si site. This
245 substitution mechanism yields several nonequivalent configurations. All
246 nonequivalent structures were investigated, and our calculations show the energy
247 difference between other nonequivalent structures and the one with the lowest total
248 energy is also large (i.e., > 0.21 eV for $Mg_{24}Al_{15}TiSi_{23}AlO_{96}$ pyrope). Similarly,
249 the structure with the lowest total energy was used. Our calculations show that the
250 energy difference between two Ti^{4+}-doped pyrope structures generated through two
251 different substitution mechanisms ($^{VI}Al^{3+}+^{IV}Si^{4+} \leftrightarrow ^{VI}Ti^{4+}+^{IV}Al^{3+}$ and $Si^{4+} \leftrightarrow Ti^{4+}$) is
252 very small (i.e., ~0.02 eV between $Mg_{24}Al_{15}TiSi_{23}AlO_{96}$ and $Mg_{24}Al_{16}TiSi_{23}O_{96}$
253 pyrope), suggesting these two substitution mechanisms are equally important for the
254 incorporation of Ti^{4+} into pyrope.

255 The Ti^{3+} incorporation into orthopyroxene and clinopyroxene through the

256 $^{VI}Mg^{2+}+^{IV}Si^{4+}\leftrightarrow{}^{VI}Ti^{3+}+^{IV}Al^{3+}$ substitution (Simon and Sutton, 2017) and into pyrope
257 through $^{VI}Al^{3+}\leftrightarrow{}^{VI}Ti^{3+}$ were also investigated. Orthopyroxene has two nonequivalent
258 Mg sites (M1 and M2). The configuration that M1-site Mg and its nearest SiB-site Si
259 are replaced by Ti and Al atoms respectively has the lowest total energy. Similarly, the
260 Ti-doped clinopyroxene generated by replacing the nearest neighbor $^{VI}Mg^{2+}$–$^{IV}Si^{4+}$
261 pair with $^{VI}Ti^{3+}$–$^{IV}Al^{3+}$ pair is the most stable one.

262 Finally, because naturally occurring silicate minerals have variable Ti contents,
263 we also calculated the structures and reduced partition function ratios of these
264 Ti-doped silicate minerals with different Ti contents. The initial structures of
265 clinopyroxene, orthopyroxene, olivine, and pyrope with different Ti contents were
266 obtained by incorporating Ti into their supercells, which were generated by expanding
267 the primitive cell along different directions. For example, the 80-atom and 320-atom
268 supercells of clinopyroxene could be obtained by expanding the primitive cell twice
269 along the c direction and twice simultaneously along a, b, c directions, respectively.
270 Substituting one Si atom with one Ti atom can produce the initial clinopyroxene
271 structures with Ti/(Ti+Si) of 1/16 and 1/64, respectively. Similarly, replacing the
272 nearest neighboring $^{VI}Mg^{2+}$–$^{IV}Si^{4+}$ pair in an 80-atom clinopyroxene supercell with
273 $^{VI}Ti^{3+}$–$^{IV}Al^{3+}$ pair could generate the initial configuration with Ti/(Ti+Si)=1/16 for the
274 $^{VI}Mg^{2+}+^{IV}Si^{4+}\leftrightarrow{}^{VI}Ti^{3+}+^{IV}Al^{3+}$ substitution. Initial structures of other minerals were
275 also produced in the same way. The supercell construction details are shown in Table
276 1.

3.2 Relaxed crystal structures

All relaxed structures of Ti-doped silicate minerals and Fe-Ti oxides, including geikielite-ilmenite solid solutions and rutile, are shown in Fig. 1 with emphases on Mg-O, Ca-O, Fe-O, Si-O, Ti-O, and Al-O polyhedrons. Their atomic positions can be found in the supplementary materials. The relaxed cell parameters are reported in Table S2. Cell parameters and volumes of geikielite, ilmenite, and rutile calculated based on LDA at static conditions agree with experimental data at 300 K within 2% (Table S2). Typically, the LDA calculation at static conditions underestimates the volume by ~1-2% because the effects of zero-point motion and room temperature on volumes have not been considered. When these effects are taken into account, the theoretical results for orthopyroxene, clinopyroxene, olivine, and pyrope are consistent with experimental data within 1% (Huang et al., 2013; Huang et al., 2014; Wu et al., 2015). There is no experimental measurement of the volumes of Ti-doped silicate minerals. Moreover, most calculated vibrational frequencies for geikielite, $FeTiO_3$ ilmenite, and rutile are also in agreements with experimental results (Table S3-S5), although some calculated frequencies significantly deviate from experimental data. These comparisons justify the reliability and accuracy of our calculations. Following Méheut et al. (2009), the uncertainty on $10^3 \ln\beta$ and $10^3 \ln\alpha$ is 3.6% and 5.0%, respectively, which are estimated based on the relationship between the calculated and measured frequencies for pure silicate minerals and Fe-Ti oxides (Table S3-S5, Huang et al., 2013).

3.3 Average Ti-O bond lengths

The calculated average Ti-O bond lengths and Ti coordination numbers (CNs) in Ti-doped silicate minerals, geikielite-ilmenite solid solutions, and rutile are listed in Table 1. The average Ti-O bond length and Ti CN depend on the arbitrarily accepted threshold of Ti-O bond lengths. Because Ti-O distances in all calculated minerals form two populations, ranging from 1.7 Å to 2.2 Å or greater than 3.0 Å, we adopted the value of 2.2 Å as the cutoff to determine Ti-O bond lengths and Ti CNs. In all silicate minerals, Ti occupying the tetrahedral Si site has a CN of four. Titanium, either Ti^{3+} or Ti^{4+}, occupying the octahedral Mg site in pyroxenes and the octahedral Al site in pyrope has a CN of 6. In Fe-Ti oxides, Ti has a CN of 6.

Ti^{4+} occupying the tetrahedral Si site in clinopyroxene, orthopyroxene, olivine, and pyrope through the $Si^{4+}\leftrightarrow Ti^{4+}$ substitution have similar average Ti-O bond lengths, which are the shortest among all calculated minerals. In contrast, Ti^{3+} occupying the octahedral Mg site in pyroxenes through the $Mg^{2+}+Si^{4+}\leftrightarrow Ti^{3+}+Al^{3+}$ substitution has the longest average Ti-O bond length. Both Ti^{4+} and Ti^{3+} can occupy the octahedral Al site in pyrope through $Al^{3+}+Si^{4+}\leftrightarrow Ti^{4+}+Al^{3+}$ and $Al^{3+}\leftrightarrow Ti^{3+}$ substitutions, respectively, but the average Ti^{4+}-O bond is significantly shorter than that of Ti^{3+}-O. The average Ti-O bond length increases in the order of: Ti^{4+}-O in silicates < Ti^{4+}-O in Fe-Ti oxides < Ti^{3+}-O in silicates.

Within the explored compositional space (Table 1), there is no significant Ti^{4+} or Ti^{3+} concentration effect on the average Ti-O bond lengths (< 0.02 Å) in silicate

minerals. In contrast, Mg or Fe concentration affect the average Ti-O bond lengths in geikielite-ilmenite solutions, from 1.9685 Å in $MgTiO_3$ to 1.9733 Å in $FeTiO_3$.

3.4 The reduced partition function ratios (10^3lnβ) of $^{49}Ti/^{47}Ti$

The 10^3lnβ of $^{49}Ti/^{47}Ti$ of all calculated minerals are shown in Fig. 2, and their polynomial fitting factors as a function of temperature are listed in Table 2. The 10^3lnβ are described using the following five categories: (1) Ti^{4+}_{Si}: Ti^{4+} occupies the tetrahedral site in pyroxenes, olivine, and pyrope; (2) Ti^{4+}_{Al}: Ti^{4+} occupies the octahedral Al site in pyrope; (3) Ti^{3+}_{Al}: Ti^{3+} occupies the octahedral Al site in pyrope; (4) Fe-Ti oxides, including geikielite-ilmenite solutions and rutile; (5) Ti^{3+}_{Mg}: Ti^{3+} occupies the octahedral Mg site in pyroxenes, olivine, and pyrope. At 1000 K, the 10^3lnβ ranges from 2.29 ‰ in Ti^{4+}_{Si}-doped olivine to 1.18 ‰ in rutile (Table 2). It decreases in the order of Ti^{4+}_{Si}-doped olivine, clinopyroxene, orthopyroxene, and pyrope > Ti^{4+}_{Al}-doped pyrope > Ti^{3+}_{Al}-doped pyrope > geikielite ($MgTiO_3$) > $Mg_{0.5}Fe_{0.5}TiO_3$ > Ti^{3+}_{Mg}-doped clinopyroxene and orthopyroxene > ilmenite ($FeTiO_3$) > rutile.

Ti^{4+}_{Si}-doped olivine, clinopyroxene, orthopyroxene, and pyrope have similar 10^3lnβ, independent of the mineral species and their Ti^{4+} contents. Likewise, Ti^{3+}_{Mg}-doped clinopyroxene and orthopyroxene have similar 10^3lnβ values, which are insensitive to their Ti^{3+} contents. In contrast, in orthopyroxene, the 10^3lnβ of $^{44}Ca/^{40}Ca$ strongly depends on the Ca concentration in orthopyroxene within a narrow Ca concentration range but become insensitive to Ca concentration when it is lower

than a threshold value (Feng et al., 2014; Wang et al., 2017a). Similar effect is also found for $10^3\ln\beta$ of $^{26}Mg/^{24}Mg$ in carbonates (Wang et al., 2017b; Wang et al., 2019). Consequently, it can be inferred that the Ti content investigated in here should be lower than the threshold concentration, below which the $10^3\ln\beta$ of $^{49}Ti/^{47}Ti$ does not vary with the Ti content in silicate minerals (Fig. 2). However, the $10^3\ln\beta$ of $^{49}Ti/^{47}Ti$ of geikielite-ilmenite solutions significantly decrease with increasing Fe content, and the difference of $10^3\ln\beta$ between $MgTiO_3$ and $FeTiO_3$ is 0.25 ‰ at 1000 K. On the other hand, the $10^3\ln\beta$ of silicate minerals are also controlled by the sites occupied by Ti. For example, at 1000 K, the difference of $10^3\ln\beta$between Ti^{4+}_{Si}-doped and Ti^{4+}_{Al}-doped pyrope is 0.45 ‰, and that between Ti^{4+}_{Si}-doped and Ti^{3+}_{Mg}-doped clinopyroxene is ~ 0.87 ‰.

4. Discussion

4.1 Controlling factors on $10^3\ln\beta$ of $^{49}Ti/^{47}Ti$

At a given temperature and pressure, mass-dependent equilibrium isotope fractionation factors are dominantly controlled by the relative bond strengths (Bigeleisen and Mayer, 1947; Urey, 1947), which are jointly determined by various factors including bond length, CN, oxidation state, and electronic configuration. In general, shorter bonds are stronger with higher vibrational frequencies and enriched in heavier isotopes relative to longer and weaker bonds (Urey, 1947; Schauble et al., 2004; Hill and Schauble, 2008; Young et al., 2009;

Huang et al., 2013; Huang et al., 2014). For instance, our previous works (Feng et al., 2014; Wang et al., 2017a, b; Li et al., 2019) have demonstrated that the 10^3lnβ of $^{26}Mg/^{24}Mg$ for carbonates, the 10^3lnβ of $^{44}Ca/^{40}Ca$ for orthopyroxene, and the 10^3lnβ of $^{41}K/^{39}K$ for feldspars are negatively correlated with their average Mg-O, Ca-O, and K-O bond lengths, respectively.

Similarly, the 10^3lnβ of $^{49}Ti/^{47}Ti$ for all calculated silicate minerals show a general negative correlation with the average Ti-O bond lengths (Fig. 3a). Within geikielite-ilmenite solid solutions, the 10^3lnβ is also linearly correlated with the average Ti-O bond length. This is mainly because geikielite-ilmenite solid solutions have similar crystal structures, so that their 10^3lnβ are dominantly controlled by the average Ti-O bond lengths. Compared to Ti^{3+}_{Mg}-doped clinopyroxene and orthopyroxene, ilmenite and rutile have shorter average Ti-O bond lengths but smaller 10^3lnβ values (Fig. 2 and Fig. 3a), although Ti is all six-fold coordinated in those minerals (Table 1). These exceptions reveal that Ti-O bond length does not perfectly describe 10^3lnβ. Other parameters are also important, including the electronegativity of the second closest atoms relative to Ti atom (the closest atom is O), which probably affect the interaction between Ti atom and its surrounding atoms. Furthermore, the valence state of Ti could also influence the 10^3lnβ. Ti^{4+} and Ti^{3+} can occupy the octahedral Al site in pyrope through the $Al^{3+}+Si^{4+}\leftrightarrow Ti^{4+}+Al^{3+}$ and $Al^{3+}\leftrightarrow Ti^{3+}$ substitutions, respectively; hence the Ti^{4+} bonding environment in pyrope should be similar to that of Ti^{3+}. Nevertheless, the 10^3lnβ of Ti^{4+}_{Al}-doped pyrope is significantly

larger than of Ti^{3+}_{Al}-doped pyrope. This is mainly because the valence state of Ti in the octahedral Al site affects the average Ti-O bond length (Table 1 and Fig. 3a).

To quantify the dominant factor of $10^3 ln\beta$, the bond strength, we calculated the average force constant of Ti, $<F>$ (in N/m) (Table 2) using the partial phonon density of state *g(E)* of Ti following Dauphas et al. (2012):

$$< F >= \frac{M}{\hbar^2} \int_0^{+\infty} E^2 g(E) dE \quad (5)$$

where *M* is the mass of Ti, and $\hbar$ is the reduced Planck constant. As shown in Fig. 3b, at 1000 K $10^3 ln\beta$ are linearly, positively correlated with $<F>$ of Ti. The $<F>$ of Ti occupying the tetrahedral Si sites in silicate minerals have a small variation and are the largest among all calculated minerals, completely explaining the largest $10^3 ln\beta$ in those Ti^{4+}_{Si}-doped silicate minerals (Table 2 and Fig. 3b). Likewise, rutile has the smallest $<F>$ of Ti, and hence it has the smallest $10^3 ln\beta$. In particular, the $<F>$ of Ti in geikielite-ilmenite solid solutions linearly decreases with increasing Fe/(Fe+Mg) (Table 2), which explains the linear correlation between the $10^3 ln\beta$ and Fe/(Fe+Mg) in geikielite-ilmenite solid solutions. Therefore, the bond strength is better measured by the average force constant, which dominantly determines $10^3 ln\beta$.

4.2 Equilibrium inter-mineral Ti isotope fractionation factors

Because clinopyroxene is a common Ti-bearing mineral in silicate rocks, it is used as a reference to report equilibrium inter-mineral Ti isotope fractionation factors ($10^3 ln\alpha$ of $^{49}Ti/^{47}Ti$). The $10^3 ln\alpha$ between minerals and Ti^{4+}_{Si}-doped clinopyroxene as a function of temperature are plotted in Fig. 4, and their polynomial fitting factors are

403 reported in Table 3. The $10^3\ln\alpha$ between other silicate minerals (olivine,
404 orthopyroxene, and pyrope) and clinopyroxene are close to zero when Ti occupies the
405 tetrahedral Si sites. At 1000 K, the $10^3\ln\alpha_{\text{mineral-clinopyroxene}}$ only ranges from 0.077 ‰
406 for olivine to -0.049 ‰ for orthopyroxene regardless of their Ti concentrations (Table
407 3). In contrast, if Ti^{4+} occupies the octahedral Al site in pyrope through the
408 $Al^{3+}+Si^{4+}\leftrightarrow Ti^{4+}+Al^{3+}$ substitution, the $10^3\ln\alpha_{\text{pyrope-clinopyroxene}}$ will be around -0.5 ‰ at
409 1000 K (Table 3). As both $Al^{3+}+Si^{4+}\leftrightarrow Ti^{4+}+Al^{3+}$ and $Si^{4+}\leftrightarrow Ti^{4+}$ substitutions are
410 important for the incorporation of Ti^{4+} into pyrope from the perspective of total
411 energy, it is inferred that pyrope is relatively enriched in light Ti isotopes compared to
412 Ti^{4+}_{Si}-doped clinopyroxene. In addition, the $10^3\ln\alpha_{\text{mineral-clinopyroxene}}$ between
413 Ti^{3+}_{Mg}-doped clinopyroxene and orthopyroxene is up to ~ -0.9 ‰ at 1000 K (Table 3),
414 indicating the extremely enrichment of light Ti isotope in Ti^{3+}-bearing species relative
415 to the Ti^{4+}-bearing minerals. This inference may be important in assessing the Ti
416 isotope data in lunar rocks (Miller et al., 2016; Simon and Sutton, 2017).

417 **4.3 Implications for Ti isotope geochemistry**

418 Krawczynski et al. (2009) demonstrated that pyroxenes and garnets could
419 contain a certain percentage of Ti^{3+} under reducing condition (e.g., 2 log units below
420 the iron–w sti te buffer). In Apollo 14 aluminous basalts 14053 and 14072, 0–60% of
421 the Ti in pyroxene are trivalent (Simon and Sutton, 2017), although most pyroxenes
422 contain little or no detectable Ti^{3+}. The pyroxene with the most reduced Ti, i.e., lowest
423 $Ti^{4+}/(Ti^{4+} + Ti^{3+})$, was thought to crystallize before plagioclase, while the pyroxene

crystallizing from the melt after plagioclase came in dominantly contains Ti^{4+} (Simon and Sutton, 2017). On the other hand, a recent experimental study conducted by Leitzke et al. (2018) also suggested that Ti^{3+} only occurs in silicate minerals. According to our results (Fig. 4), the Ti^{3+}-bearing lunar pyroxene should be enriched light Ti isotopes relative to other Ti^{4+}-bearing pyroxenes, a prediction to be tested by future study. Moreover, some pyroxenes in refractory inclusions in chondrites have a $Ti^{3+}/(Ti^{3+}+Ti^{4+})$ ratio of ~ 0.4 (Simon et al., 2007), and some ordinary and enstatite chondrites are also enriched in Ti^{3+} (Simon et al., 2016). Thus, due to the large $10^3 ln\alpha$ between Ti^{3+} and Ti^{4+} species, Ti isotopes could be fractionated by the change of redox state during the thermal metamorphism processes on ordinary and enstatite chondrite parental bodies. Hence, Ti isotope composition can trace the thermal metamorphism process.

However, negligible Ti^{3+} has been detected in terrestrial samples that originate from more oxidizing environment relative to the iron–w sti te buffer, suggesting that the Ti^{3+} species have a negligible contribution to the Ti isotope variation in terrestrial samples (Millet et al., 2016; Greber et al., 2017a, b; Deng et al., 2019). In contrast, Fe-Ti oxides (such as ilmenite and magnetite) play a key role in Ti isotope systematics during magma differentiation (Millet et al., 2016; Greber et al., 2017a, b; Deng et al., 2019). They suggested that Fe-Ti oxides should be enriched in light Ti isotopes relative to the melt, but different Ti isotopic fractionation factors between Fe-Ti oxides and melt ($\Delta^{49}Ti^{oxides\text{-}melt}$) were inferred. In detail, Millet et al. (2016) found that

445 the $\Delta^{49}Ti^{oxides\text{-}melt} = -0.23\times10^6/T^2$ (T is temperature in Kelvin) based on the Agung
446 volcanic samples with a SiO_2 range of 54-65 wt.%. In contrast, based on Hekla lavas
447 with a wide SiO_2 range of 46.47-72.07 wt.%, Deng et al. (2019) proposed that the
448 $\Delta^{49}Ti^{oxides\text{-}melt}$ should be ~-0.1‰ at ~1500 K and ~-0.5‰ at ~1150 K, which
449 indicates that $\Delta^{49}Ti^{oxides\text{-}melt}$ is not only controlled by temperature. Deng et al.
450 (2019) speculated that the change of silicate melt structure with increasing SiO_2
451 contents causes the variation in $\Delta^{49}Ti^{oxides\text{-}melt}$ (Farges and Brown, 1997). Thus, the
452 temperature dependence of $\Delta^{49}Ti^{oxides\text{-}melt}$ in Millet et al. (2016) is only valid for melt
453 with low SiO_2 content. In fact, $\Delta^{49}Ti^{oxides\text{-}melt}$ is a function of both temperature and
454 melt SiO_2 content (Deng et al., 2019).

455 Our results show that the $10^3\ln\alpha$ between ilmenite and Ti^{4+}_{Si}-doped
456 clinopyroxene is up to -0.67‰ at 1200 K. Because estimating the $10^3\ln\beta$ of melts is
457 still a challenge, the $10^3\ln\alpha$ between ilmenite and silicate melt needs to be determined
458 in future study. As the local structure of Ti in silicate melt is different from the one in
459 Ti^{4+}_{Si}-doped clinopyroxene (Farges and Brown, 1997), Ti isotope fractionation
460 between the melt and Ti^{4+}_{Si}-doped silicate minerals could be significant, and the
461 $10^3\ln\alpha$ between ilmenite and Ti^{4+}_{Si}-doped clinopyroxene cannot be simply taken as
462 the one between ilmenite and silicate melt. However, our calculations show that the
463 $10^3\ln\alpha$ between geikielite-ilmenite solid solutions and Ti^{4+}_{Si}-doped clinopyroxene
464 significantly decreases with increasing Mg/(Fe+Mg) ratio in geikielite-ilmenite solid
465 solutions, with $10^3\ln\alpha_{MgTiO3\text{-}clinopyroxene}$ up to -0.49 ‰ at 1200 K (Table 3 and Fig. 4).

Thus, the $10^3\ln\alpha$ between ilmenite and melt is controlled by both the melt structure (SiO_2 content) and the composition of geikielite-ilmenite solid solutions. Additionally, Ti-magnetite, with a large variable composition range, also plays an important role controlling Ti isotope behaviors during magma differentiation, because it is a major Fe-Ti oxide during terrestrial basaltic magma evolution compared to ilmenite (e.g., Helz, 1987; Zhang et al., 2018). It is expected that the $10^3\ln\beta$ of magnetite is significantly affected by its Ti content, and hence the $10^3\ln\alpha$ between magnetite and silicate melt is also controlled by the Ti content in magnetite. As a consequence, the chemical composition of Fe-Ti oxides may significantly contribute to the Ti isotopic variability found in natural rocks (Millet et al., 2016; Greber et al., 2017a, b; Deng et al., 2019). Further studies on the $10^3\ln\beta$ of Ti-magnetite are required for a better understanding of the role of Fe-Ti oxides controlling the Ti isotope composition during magma evolution.

4.4 A potential Ti isotope thermometer

Temperature is an important parameter controlling magma evolution. Deng et al. (2019) estimated the temperatures during fractional crystallization of Fe-Ti oxides by calculating liquidus temperatures of the samples using rhyolite-melts with an assumed pressure and pre-eruptive H_2O/K_2O ratio. Our results demonstrate that the large $10^3\ln\alpha$ of $^{49}Ti/^{47}Ti$ between ilmenite and clinopyroxene can be used to evaluate whether the Ti isotope exchange in natural samples have reached the equilibrium state or not. The relationship between $10^3\ln\alpha_{ilmenite\text{-}clinopyroxene}$ and temperature can be further

used to independently determine the equilibrium temperature (Fig. 5). For example, the estimated $10^3\ln\alpha_{FeTiO3\text{-}clinopyroxene}$ ranging from -0.91 ‰ to -0.47 ‰ corresponds to temperature increasing from 1000 K to 1400 K. Since the $10^3\ln\alpha_{ilmenite\text{-}clinopyroxene}$ is not only controlled by temperature but also significantly depends on its Mg/(Fe+Mg) ratio, the determination of chemical composition of ilmenite is important for the accurate temperature estimation. Standard error of the estimation (SEE) of temperature can be estimated based on the combination of current analytical precision of Ti isotope composition (Millet and Dauphas, 2014) and the uncertainty of our calculated inter-mineral fractionation factor. Here we assumed that the analytical uncertainty for Ti isotope measurements of minerals is the same to the level of current analytical precision of Ti isotope composition (Millet and Dauphas, 2014). For instance, if the relationship between $10^3\ln\alpha_{FeTiO3\text{-}clinopyroxene}$ and temperature is adopted, the standard error at 1200 K is about 40 K, which is comparable to that of the elemental geothermometer (Putirka, 2008, 2016). Consequently, the inter-mineral Ti isotope fractionation between ilmenite and clinopyroxene could provide independent constraint on the equilibrium temperature.

5. Conclusions

This study presents the first investigation of equilibrium inter-mineral Ti isotope fractionation among a large number of silicate minerals and Fe-Ti oxides based on the DFT. Our results find large variation in $10^3\ln\beta$ of $^{49}Ti/^{47}Ti$. It decreases in the order of

508 Ti^{4+}_{Si}-doped olivine, clinopyroxene, orthopyroxene, and pyrope > Ti^{4+}_{Al}-doped
509 pyrope > Ti^{3+}_{Al}-doped pyrope > geikielite ($MgTiO_3$) > $Mg_{0.5}Fe_{0.5}TiO_3$ > Ti^{3+}_{Mg}-doped
510 clinopyroxene and orthopyroxene > ilmenite ($FeTiO_3$) > rutile. The $10^3 ln\beta$ of
511 Ti^{4+}_{Si}-doped and Ti^{3+}_{Mg}-doped silicate minerals are not sensitive to their Ti^{4+} and Ti^{3+}
512 contents, respectively. However, the $10^3 ln\beta$ of geikielite-ilmenite solutions
513 significantly decrease with increasing Fe/(Fe+Mg) ratio. Notably, the $10^3 ln\beta$ is
514 linearly, positively correlated to the Ti force constant, which is significantly affected
515 by the average Ti-O bond length and the valence state of Ti.

516 There is no significant Ti isotope fractionation among Ti^{4+}_{Si}-doped
517 clinopyroxene, orthopyroxene, olivine, and pyrope. However, redox condition plays
518 an important role fractionating Ti isotopes. Specifically, Ti^{3+}_{Mg}-doped clinopyroxene
519 and orthopyroxene are extremely enriched in light Ti isotopes relative to those
520 Ti^{4+}_{Si}-doped species. Consequently, Ti isotopes might be able to trace redox condition
521 under extremely reducing conditions, such as that during the lunar magma ocean
522 evolution and enstatite chondrite formation. In terrestrial samples, Fe-Ti oxides (such
523 as ilmenite) play a key role fractionating Ti isotopes during magma differentiation.
524 Our calculations demonstrate the enrichment of light Ti isotopes in ilmenite relative to
525 Ti^{4+}_{Si}-doped silicate minerals with $10^3 ln\alpha_{FeTiO3\text{-}clinopyroxene}$ of $^{49}Ti/^{47}Ti$ is up to -0.67‰
526 at 1200 K. In particular, the $10^3 ln\alpha$ between Fe-Ti oxides and melt also strongly
527 depends on the chemical composition of Fe-Ti oxides, which may significantly
528 contribute to the Ti isotopic variability during magma differentiation. In addition, the

529 inter-mineral Ti isotope fractionation between ilmenite and clinopyroxene can be used
530 as a thermometer, with the estimated temperature precision comparable to that of
531 elemental geothermometer if the analytical uncertainty for Ti isotope measurements
532 of minerals is the same to the level of current analytical precision of Ti isotope
533 composition.
534
535 **Acknowledgments**
536 This work is supported by the Strategic Priority Research Program (B) of the Chinese
537 Academy of Sciences (grant XDB18000000), Natural Science Foundation of China
538 (41590621, 41473011, 41721002), 111 Project and Special Program for Applied
539 Research on Super Computation of the NSFC-Guangdong Joint Fund. SH
540 acknowledges support from NSF EAR-1524387. Some computations were conducted
541 in the Supercomputing Center of the University of Science and Technology of China.

Tables

Table 1. Average Ti-O bond lengths, coordination numbers, and force constant of Ti in major silicate minerals, geikielite-ilmenite solid solutions, and rutile.

Minerals	Chemical composition	Ti content	Average Ti-O bond length (Å)	CN	Force constant (N/m)
clinopyroxene $Si^{4+}\leftrightarrow Ti^{4+}$	$Mg_8Ca_8Si_{15}TiO_{48}$	Ti/(Ti+Si)=1/16, 2c	1.8139	4	586.8
	$Mg_{16}Ca_{16}Si_{31}TiO_{96}$	Ti/(Ti+Si)=1/32, 2b, 2c	1.8126	4	596.2
	$Mg_{24}Ca_{24}Si_{47}TiO_{144}$	Ti/(Ti+Si)=1/48, 2b, 3c	1.8133	4	591.6
	$Mg_{32}Ca_{32}Si_{63}TiO_{192}$	Ti/(Ti+Si)=1/64, 2a, 2b, 2c	1.8127	4	591.8
clinopyroxene $Mg^{2+}+Si^{4+}\leftrightarrow Ti^{3+}+Al^{3+}$	$Mg_7TiCa_8Si_{15}AlO_{48}$	Ti/(Ti+Si)=1/16, 2c	2.0489	6	352.6
	$Mg_{15}TiCa_{16}Si_{31}AlO_{96}$	Ti/(Ti+Si)=1/32, 2b, 2c	2.0491	6	356.9
orthopyroxene $Si^{4+}\leftrightarrow Ti^{4+}$	$Mg_{16}Si_{15}TiO_{48}$	Ti/(Ti+Si)=1/16	1.8176	4	587.2
	$Mg_{32}Si_{31}TiO_{96}$	Ti/(Ti+Si)=1/32, 2c	1.8181	4	584.5
	$Mg_{48}Si_{47}TiO_{144}$	Ti/(Ti+Si)=1/48, 3c	1.8189	4	578.5
	$Mg_{64}Si_{63}TiO_{192}$	Ti/(Ti+Si)=1/64, 2b, 2c	1.8182	4	580.4
orthopyroxene $Mg^{2+}+Si^{4+}\leftrightarrow Ti^{3+}+Al^{3+}$	$Mg_{15}TiSi_{15}AlO_{48}$	Ti/(Ti+Si)=1/16	2.0438	6	354.3
	$Mg_{31}TiSi_{31}AlO_{96}$	Ti/(Ti+Si)=1/32, 2c	2.0448	6	352.7
olivine $Si^{4+}\leftrightarrow Ti^{4+}$	$Mg_{32}Si_{15}TiO_{64}$	Ti/(Ti+Si)=1/16, 2a, 2c	1.8100	4	604.4
	$Mg_{64}Si_{31}TiO_{128}$	Ti/(Ti+Si)=1/32, 2a, 2b, 2c	1.8095	4	611.2
pyrope $Al^{3+}+Si^{4+}\leftrightarrow Ti^{4+}+Al^{3+}$	$Mg_{12}Al_7TiSi_{11}AlO_{48}$	Ti/(Ti+Si+Al)=1/20[#]	1.9306	6	446.5
	$Mg_{24}Al_{15}TiSi_{23}AlO_{96}$	Ti/(Ti+Si+Al)=1/40[*]	1.9286	6	457.1
$Si^{4+}\leftrightarrow Ti^{4+}$	$Mg_{24}Al_{16}Si_{23}TiO_{96}$	Ti/(Ti+Si+Al)=1/40[*]	1.8083	4	578.6
$Al^{3+}\leftrightarrow Ti^{3+}$	$Mg_{24}Al_{15}TiSi_{24}O_{96}$	Ti/(Ti+Si+Al)=1/40[*]	1.9961	6	423.0
geikielite	$Mg_6Ti_6O_{18}$		1.9685	6	399.4
	$Mg_3Fe_3Ti_6O_{18}$		1.9717	6	370.0
ilmenite	$Fe_6Ti_6O_{18}$		1.9733	6	332.5
rutile	Ti_2O_4		1.9535	6	314.2

Abbreviations after Ti contents refer to the expansion way of primitive cells to generate supercells. For instance, "2a, 2b, 2c" represents the supercell is generated by expanding the primitive cell twice along a, b, and c directions. [#], the primitive cell of pyrope (80 atoms); [*], the conventional cell of pyrope (160 atoms)

549 **Table 2.** Polynomial fitting parameters of the reduced partition function ratios (10^3lnβ)
550 of $^{49}Ti/^{47}Ti$ for Ti-doped silicate minerals, geikielite-ilmenite solid solutions, and
551 rutile.

clinopyroxene	chemical composition	Ti content	*a*	*b*	*c*
$Si^{4+}\leftrightarrow Ti^{4+}$	$Mg_8Ca_8Si_{15}TiO_{48}$	Ti/(Ti+Si)=1/16	2.23693	-4.097E-02	1.184E-03
	$Mg_{16}Ca_{16}Si_{31}TiO_{96}$	Ti/(Ti+Si)=1/32	2.27279	-4.163E-02	1.202E-03
	$Mg_{24}Ca_{24}Si_{47}TiO_{144}$	Ti/(Ti+Si)=1/48	2.25319	-4.127E-02	1.192E-03
	$Mg_{32}Ca_{32}Si_{63}TiO_{192}$	Ti/(Ti+Si)=1/64	2.25653	-4.133E-02	1.194E-03
$Mg^{2+}+Si^{4+}\leftrightarrow Ti^{3+}+Al^{3+}$	$Mg_7TiCa_8Si_{15}AlO_{48}$	Ti/(Ti+Si)=1/16	1.34285	-1.101E-02	1.906E-04
	$Mg_{15}TiCa_{16}Si_{31}AlO_{96}$	Ti/(Ti+Si)=1/32	1.36027	-1.115E-02	1.929E-04
orthopyroxene					
$Si^{4+}\leftrightarrow Ti^{4+}$	$Mg_{16}Si_{15}TiO_{48}$	Ti/(Ti+Si)=1/16	2.23666	-4.057E-02	1.166E-03
	$Mg_{32}Si_{31}TiO_{96}$	Ti/(Ti+Si)=1/32	2.22630	-4.038E-02	1.161E-03
	$Mg_{48}Si_{47}TiO_{144}$	Ti/(Ti+Si)=1/48	2.20346	-3.997E-02	1.149E-03
	$Mg_{64}Si_{63}TiO_{192}$	Ti/(Ti+Si)=1/64	2.21084	-4.010E-02	1.153E-03
$Mg^{2+}+Si^{4+}\leftrightarrow Ti^{3+}+Al^{3+}$	$Mg_{15}TiSi_{15}AlO_{48}$	Ti/(Ti+Si)=1/16	1.34287	-1.072E-02	1.775E-04
	$Mg_{31}TiSi_{31}AlO_{96}$	Ti/(Ti+Si)=1/32	1.33676	-1.067E-02	1.767E-04
olivine					
$Si^{4+}\leftrightarrow Ti^{4+}$	$Mg_{32}Si_{15}TiO_{64}$	Ti/(Ti+Si)=1/16	2.30449	-4.059E-02	1.080E-03
	$Mg_{64}Si_{31}TiO_{128}$	Ti/(Ti+Si)=1/32	2.33041	-4.105E-02	1.092E-03
pyrope					
$Al^{3+}+Si^{4+}\leftrightarrow Ti^{4+}+Al^{3+}$	$Mg_{12}Al_7TiSi_{11}AlO_{48}$	Ti/(Ti+Si+Al)=1/20	1.70195	-1.864E-02	3.799E-04
	$Mg_{24}Al_{15}TiSi_{23}AlO_{96}$	Ti/(Ti+Si+Al)=1/40	1.74244	-1.908E-02	3.889E-04
$Si^{4+}\leftrightarrow Ti^{4+}$	$Mg_{24}Al_{16}Si_{23}TiO_{96}$	Ti/(Ti+Si+Al)=1/40	2.20599	-4.040E-02	1.167E-03
$Al^{3+}\leftrightarrow Ti^{3+}$	$Mg_{24}Al_{15}TiSi_{24}O_{96}$	Ti/(Ti+Si+Al)=1/40	1.61237	-1.766E-02	3.600E-04
geikielite-ilmenite					
Geikielite	$Mg_6Ti_6O_{18}$		1.52316	-1.492E-02	2.649E-04
	$Mg_3Fe_3Ti_6O_{18}$		1.41088	-1.226E-02	1.937E-04
ilmenite	$Fe_6Ti_6O_{18}$		1.26749	-9.644E-03	1.352E-04
rutile	Ti_2O_4		1.19767	-9.585E-03	1.543E-04

552 Polynomial fitting equation is: $10^3\ln\beta=ax+bx^2+cx^3$, where $x=10^6/T^2$. T is temperature

553 in Kelvin. Temperature range for polynomial fittings is from 673 K to 2500 K.

554 **Table 3.** Polynomial fitting parameters of the equilibrium Ti isotope fractionation
555 (10^3lnα of $^{49}Ti/^{47}Ti$) between other minerals and clinopyroxene with the chemical
556 composition of $Mg_{24}Ca_{24}Si_{47}TiO_{144}$. When Ti is incorporated into the clinopyroxene
557 through the $Si^{4+}\leftrightarrow Ti^{4+}$ substitution, Ti concentration in clinopyroxene does not show
558 significant effect on the 10^3lnα.

clinopyroxene	chemical composition	Ti content	*a*	*b*	*c*
$Mg^{2+}+Si^{4+}\leftrightarrow Ti^{3+}+Al^{3+}$	$Mg_7TiCa_8Si_{15}AlO_{48}$	Ti/(Ti+Si)=1/16	-0.91034	3.026E-02	-1.001E-03
	$Mg_{15}TiCa_{16}Si_{31}AlO_{96}$	Ti/(Ti+Si)=1/32	-0.89292	3.012E-02	-9.991E-04
orthopyroxene					
$Si^{4+}\leftrightarrow Ti^{4+}$	$Mg_{16}Si_{15}TiO_{48}$	Ti/(Ti+Si)=1/16	-0.01653	7.000E-05	-2.600E-05
	$Mg_{32}Si_{31}TiO_{96}$	Ti/(Ti+Si)=1/32	-0.02689	8.900E-04	-3.100E-05
	$Mg_{48}Si_{47}TiO_{144}$	Ti/(Ti+Si)=1/48	-0.04973	1.300E-03	-4.300E-05
	$Mg_{64}Si_{63}TiO_{192}$	Ti/(Ti+Si)=1/64	-0.04235	1.170E-03	-3.900E-05
$Mg^{2+}+Si^{4+}\leftrightarrow Ti^{3+}+Al^{3+}$	$Mg_{15}TiSi_{15}AlO_{48}$	Ti/(Ti+Si)=1/16	-0.91032	3.055E-02	-1.015E-03
	$Mg_{31}TiSi_{31}AlO_{96}$	Ti/(Ti+Si)=1/32	-0.91643	3.060E-02	-1.015E-03
olivine					
$Si^{4+}\leftrightarrow Ti^{4+}$	$Mg_{32}Si_{15}TiO_{64}$	Ti/(Ti+Si)=1/16	0.05130	6.800E-04	-1.120E-04
	$Mg_{64}Si_{31}TiO_{128}$	Ti/(Ti+Si)=1/32	0.07722	2.200E-04	-1.000E-04
pyrope					
$Al^{3+}+Si^{4+}\leftrightarrow Ti^{4+}+Al^{3+}$	$Mg_{12}Al_7TiSi_{11}AlO_{48}$	Ti/(Ti+Si+Al)=1/20	-0.55124	2.263E-02	-8.121E-04
	$Mg_{24}Al_{15}TiSi_{23}AlO_{96}$	Ti/(Ti+Si+Al)=1/40	-0.51075	2.219E-02	-8.031E-04
$Si^{4+}\leftrightarrow Ti^{4+}$	$Mg_{24}Al_{16}Si_{23}TiO_{96}$	Ti/(Ti+Si+Al)=1/40	-0.04720	8.700E-04	-2.500E-05
$Al^{3+}\leftrightarrow Ti^{3+}$	$Mg_{24}Al_{15}TiSi_{24}O_{96}$	Ti/(Ti+Si+Al)=1/40	-0.64082	2.361E-02	-8.320E-04
geikielite-ilmenite					
Geikielite	$Mg_6Ti_6O_{18}$		-0.73003	2.635E-02	-9.271E-04
	$Mg_3Fe_3Ti_6O_{18}$		-0.84231	2.901E-02	-9.983E-04
ilmenite	$Fe_6Ti_6O_{18}$		-0.98570	3.163E-02	-1.057E-03
rutile	Ti_2O_4		-1.05552	3.169E-02	-1.038E-03

559 Polynomial fitting equation is: $10^3\ln\alpha = ax + bx^2 + cx^3$, where $x = 10^6/T^2$. T is temperature
560 in Kelvin. Temperature range for polynomial fittings is from 673 K to 2500 K.

Figures

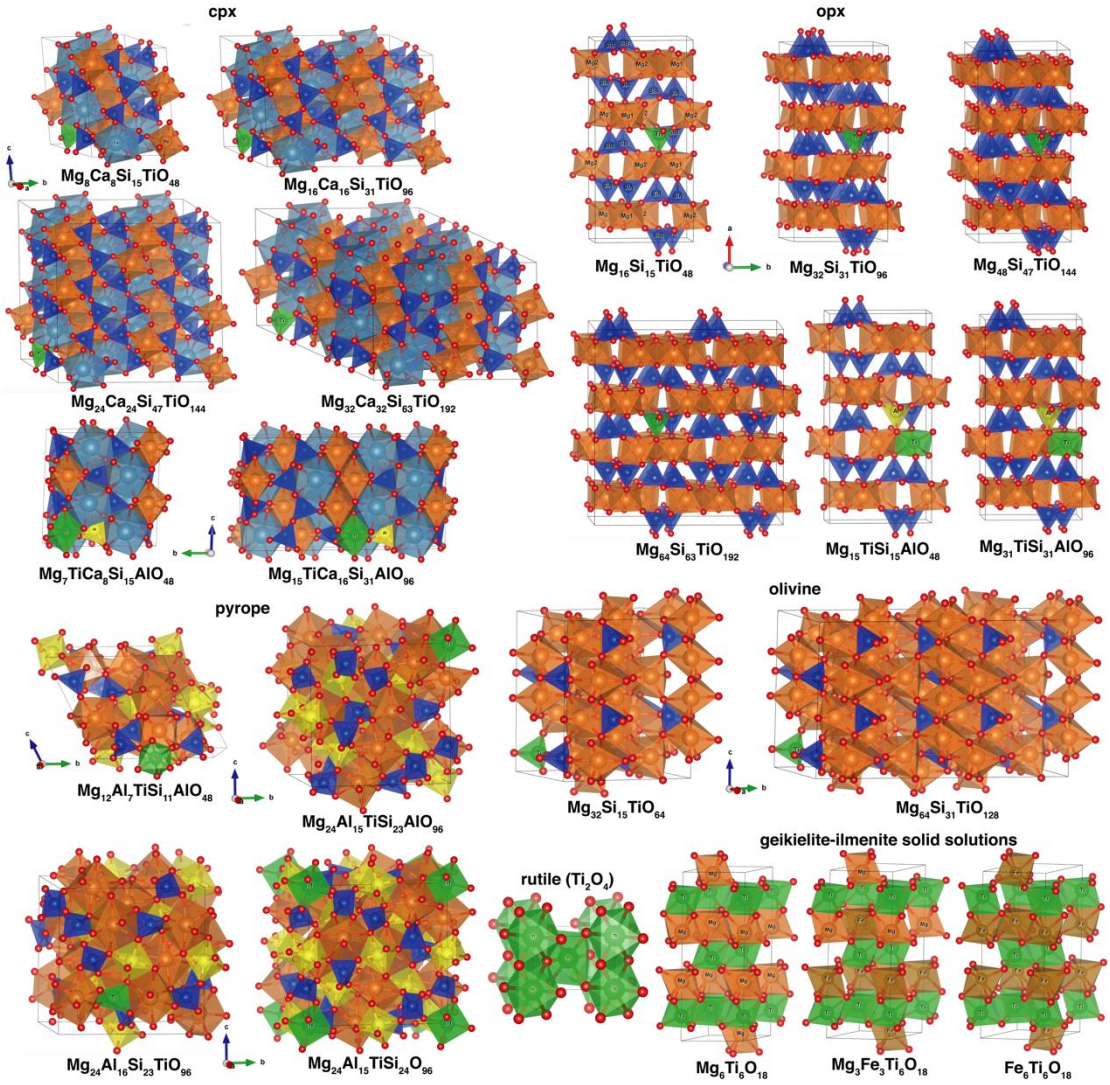

Figure 1. Relaxed crystal structures of Ti-doped clinopyroxene, orthopyroxene, olivine, pyrope, geikielite-ilmenite solid solutions ($MgTiO_3$, $Mg_{0.5}Fe_{0.5}TiO_3$, and $FeTiO_3$), and rutile (TiO_2). All crystal structures are drawn using the software "VESTA" (Momma and Izumi, 2008). Atomic colors: Ca, cyan; Mg, brown; Fe, dark brown; Si, blue; Ti, green; Al, yellow; O, red.

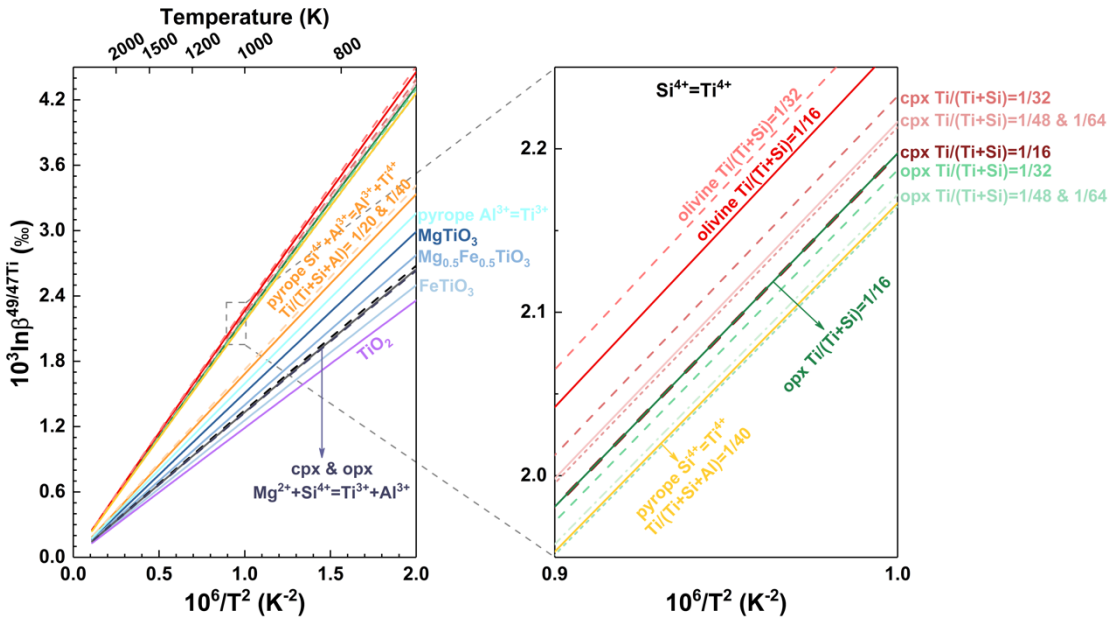

Figure 2. Temperature dependences of calculated reduced partition function ratios of $^{49}Ti/^{47}Ti$ ($10^3 ln\beta$) for clinopyroxene (cpx), orthopyroxene (cpx), olivine, pyrope, geikielite-ilmenite solid solutions ($MgTiO_3$, $Mg_{0.5}Fe_{0.5}TiO_3$, and $FeTiO_3$), and rutile (TiO_2).

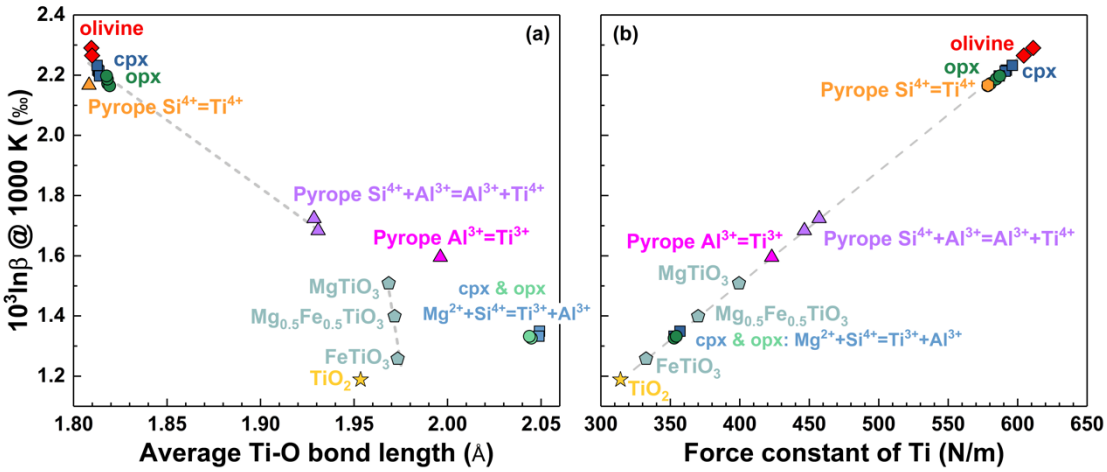

573

574 **Figure 3.** (a) The relationship between $10^3 \ln\beta$ $^{49}Ti/^{47}Ti$ at 1000 K and average Ti-O

575 bond length. (b) The linear correlation between $10^3 \ln\beta$ $^{49}Ti/^{47}Ti$ at 1000 K and force

576 constant of Ti in all calculated minerals. The coordination numbers (CN) of Ti in

577 clinopyroxene (cpx), olivine, and orthopyroxene (opx) are four, because one Ti atom

578 is incorporated into the Si tetrahedral site in these mineral structures. The CN of Ti in

579 pyrope depends on the substitution mechanism. Similarly, the CN of Ti is also four if

580 Ti is incorporated into the Si tetrahedral site in pyrope, and Ti atom is six-coordinated

581 when Ti atom occupies the Al octahedral site. The CNs of Ti in geikielite-ilmenite

582 solid solutions ($MgTiO_3$, $Mg_{0.5}Fe_{0.5}TiO_3$, and $FeTiO_3$) and rutile (TiO_2) are six.

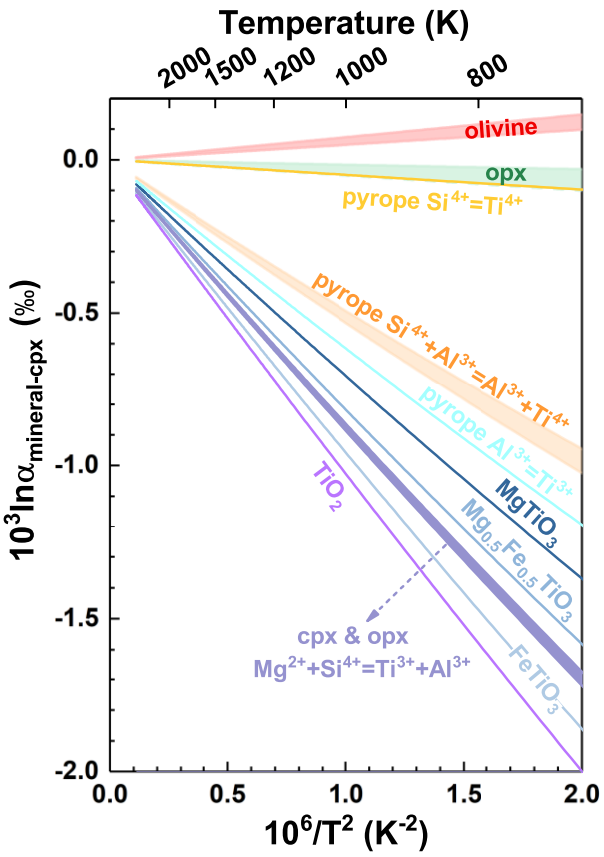

583

584 **Figure 4.** Equilibrium Ti isotope fractionation factors ($10^3\ln\alpha$) between other minerals

585 and clinopyroxene (cpx). The narrow red, green, and yellow regions represent

586 $10^3\ln\alpha_{\text{olivine-clinopyroxene}}$, $10^3\ln\alpha_{\text{orthopyroxene-clinopyroxene}}$, and $10^3\ln\alpha_{\text{pyrope-clinopyroxene}}$,

587 respectively.

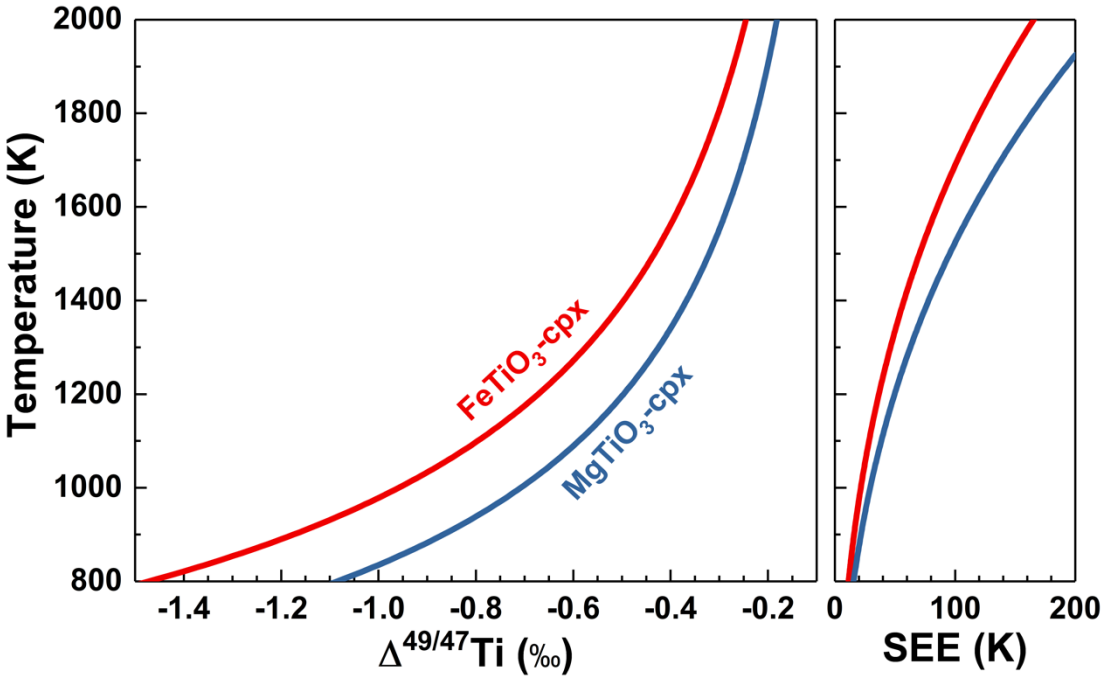

588

589 **Figure 5.** Relationship between temperature and $\Delta^{49/47}$Ti between (Fe, Mg)TiO_3 and

590 clinopyroxene as a potential Ti isotope thermometer. The Ti-doped clinopyroxene

591 structure that accommodates one Ti atom into the tetrahedral Si site through the

592 $Si^{4+}\leftrightarrow Ti^{4+}$ substitution is selected as the representative, because the Ti^{3+} content is

593 negligible in naturally occurring terrestrial samples (Millet et al., 2016). When Ti^{4+} is

594 incorporated into the clinopyroxene through the $Si^{4+}\leftrightarrow Ti^{4+}$ substitution, Ti

595 concentration in clinopyroxene does not show significant effect on its $10^3 ln\beta$ of

596 $^{49}Ti/^{47}Ti$. SEE refers to standard error of the estimation. Red and blue lines represent

597 ilmenite and geikielite, respectively.

References

Ackerson M. R., Watson E. B., Tailby N. D. and Spear F. S. (2017) Experimental investigation into the substitution mechanisms and solubility of Ti in garnet. *Am. Mineral.* **102**, 158–172.

Anders E. and Grevesse N. (1989) Abundances of the elements: Meteoritic and solar. *Geochim. Cosmochim. Acta* **53**, 197–214.

Anisimov V. I., Zaanen J. and Andersen O. K. (1991) Band theory and Mott insulators: Hubbard U instead of Stoner I. *Phys. Rev. B* **44**, 943–954.

Armbruster T. and Geiger C. A. (1993) Andradite crystal chemistry, dynamic X-site disorder and structural strain in silicate garnets. *Eur. J. Mineral.* **5**, 59–72.

Arroyo-De Dompablo M. E., Morales-Garca A. and Taravillo M. (2011) DFT+U calculations of crystal lattice, electronic structure, and phase stability under pressure of TiO_2 polymorphs. *J. Chem. Phys.* **135**.

Berry A. J., Walker A. M., Hermann J., O'Neill H. S. C., Foran G. J. and Gale J. D. (2007) Titanium substitution mechanisms in forsterite. *Chem. Geol.* **242**, 176–186.

Bigeleisen J. and Mayer M. G. (1947) Calculation of Equilibrium Constants for Isotopic Exchange Reactions. *J. Chem. Phys.* **15**, 261.

Cococcioni M. and de Gironcoli S. (2005) Linear response approach to the calculation of the effective interaction parameters in the LDA+U method. *Phys. Rev. B* **71**, 035105.

Curnan M. T. and Kitchin J. R. (2015) Investigating the Energetic Ordering of Stable and Metastable TiO_2 Polymorphs Using DFT+U and Hybrid Functionals. *J. Phys. Chem. C* **119**, 21060–21071.

Dauphas N., Roskosz M., Alp E. E., Golden D. C., Sio C. K., Tissot F. L. H., Hu M. Y., Zhao J., Gao L. and Morris R. V. (2012) A general moment NRIXS approach to the determination of equilibrium Fe isotopic fractionation factors: Application to goethite and jarosite. *Geochim. Cosmochim. Acta* **94**, 254–275.

Davis A. M., Zhang J., Greber N. D., Hu J., Tissot F. L. H. and Dauphas N. (2018) Titanium isotopes and rare earth patterns in CAIs: Evidence for thermal processing and gas-dust decoupling in the protoplanetary disk. *Geochim. Cosmochim. Acta* **221**, 275–295.

Deng Z., Chaussidon M., Savage P., Robert F., Pik R. and Moynier F. (2019) Titanium isotopes as a tracer for the plume or island arc affinity of felsic rocks. *Proc. Natl. Acad. Sci.*, 201809164.

Deng Z, Moynier F., Sossi P. A. and Chaussidon M. (2018) Bridging the depleted MORB mantle and the continental crust using titanium isotopes. *Geochemical Perspect. Lett.*, 11–15.

Deng Zhengbin, Moynier F., van Zuilen K., Sossi P. A., Pringle E. A. and Chaussidon M. (2018) Lack of resolvable titanium stable isotopic variations in bulk chondrites. *Geochim. Cosmochim. Acta* **239**, 409–419.

Farges F. and Brown G. E. (1997) Coordination chemistry of titanium (IV) in silicate

glasses and melts: IV. XANES studies of synthetic and natural volcanic glasses and tektites at ambient temperature and pressure. *Geochim. Cosmochim. Acta* **61**, 1863–1870.

Feng C., Qin T., Huang S., Wu Z. and Huang F. (2014) First-principles investigations of equilibrium calcium isotope fractionation between clinopyroxene and Ca-doped orthopyroxene. *Geochim. Cosmochim. Acta* **143**, 132–142.

Fujii T., Moynier F., Pons M.-L. and Albarède F. (2011) The origin of Zn isotope fractionation in sulfides. *Geochim. Cosmochim. Acta* **75**, 7632–7643.

Gao G. Y., Yao K. L. and Liu Z. L. (2006) First-principles study on magnetism and electronic structure of V-doped rutile TiO_2. *Phys. Lett. Sect. A Gen. At. Solid State Phys.* **359**, 523–527.

Gerke T. L., Kilinc A. I. and Sack R. O. (2005) Ti-content of high-Ca pyroxenes as a petrogenetic indicator: an experimental study of Mafic Alkaline Rocks from the Mt. Erebus volcanic region, Antarctica. *Contrib. to Mineral. Petrol.* **148**, 735–745.

Giannozzi P., Baroni S., Bonini N., Calandra M., Car R., Cavazzoni C., Ceresoli D., Chiarotti G. L., Cococcioni M., Dabo I., Dal Corso A., de Gironcoli S., Fabris S., Fratesi G., Gebauer R., Gerstmann U., Gougoussis C., Kokalj A., Lazzeri M., Martin-Samos L., Marzari N., Mauri F., Mazzarello R., Paolini S., Pasquarello A., Paulatto L., Sbraccia C., Scandolo S., Sclauzero G., Seitsonen A. P., Smogunov A., Umari P. and Wentzcovitch R. M. (2009) QUANTUM ESPRESSO: a modular and open-source software project for quantum simulations of materials. *J. Phys. Condens. Matter* **21**, 395502.

Greber Nicolas D., Dauphas N., Bekker A., Ptáček M. P., Bindeman I. N. and Hofmann A. (2017) Titanium isotopic evidence for felsic crust and plate tectonics 3.5 billion years ago. *Science* **357**, 1271–1274.

Greber Nicolas D, Dauphas N., Puchtel I. S., Hofmann B. A. and Arndt N. T. (2017) Titanium stable isotopic variations in chondrites, achondrites and lunar rocks. *Geochim. Cosmochim. Acta* **213**, 534–552.

Grew E. S., Locock A. J., Mills S. J., Galuskina I. O., Galuskin E. V. and Halenius U. (2013) Nomenclature of the garnet supergroup. *Am. Mineral.* **98**, 785–811.

Gwalani L. G., Rock N. M. S., Ramasamy R., Griffin B. J. and Mulai B. P. (2000) Complexly zoned Ti-rich melanite-schorlomite garnets from Ambadungar carbonatite-alkalic complex, Deccan Igneous Province, Gujarat State, Western India. *J. Asian Earth Sci.* **18**, 163–176.

Hermann J., O'Neill H. S. C. and Berry A. J. (2005) Titanium solubility in olivine in the system TiO_2–MgO–SiO_2: no evidence for an ultra-deep origin of Ti-bearing olivine. *Contrib. to Mineral. Petrol.* **148**, 746–760.

Hill P. S. and Schauble E. A. (2008) Modeling the effects of bond environment on equilibrium iron isotope fractionation in ferric aquo-chloro complexes. *Geochim. Cosmochim. Acta* **72**, 1939–1958.

Huang F., Chen L., Wu Z. and Wang W. (2013) First-principles calculations of

equilibrium Mg isotope fractionations between garnet, clinopyroxene, orthopyroxene, and olivine: Implications for Mg isotope thermometry. *Earth Planet. Sci. Lett.* **367**, 61–70.

Huang F., Wu Z., Huang S. and Wu F. (2014) First-principles calculations of equilibrium silicon isotope fractionation among mantle minerals. *Geochim. Cosmochim. Acta* **140**, 509–520.

Huang F., Zhou C., Wang W., Kang J. and Wu Z. (2019) First-principles calculations of equilibrium Ca isotope fractionation: Implications for oldhamite formation and evolution of lunar magma ocean. *Earth Planet. Sci. Lett.* **510**, 153–160.

Kööp L., Davis A. M., Nakashima D., Park C., Krot A. N., Nagashima K., Tenner T. J., Heck P. R. and Kita N. T. (2016a) A link between oxygen, calcium and titanium isotopes in26Al-poor hibonite-rich CAIs from Murchison and implications for the heterogeneity of dust reservoirs in the solar nebula. *Geochim. Cosmochim. Acta* **189**, 70–95.

Kööp L., Nakashima D., Heck P. R., Kita N. T., Tenner T. J., Krot A. N., Nagashima K., Park C. and Davis A. M. (2016b) New constraints on the relationship between ^{26}Al and oxygen, calcium, and titanium isotopic variation in the early Solar System from a multielement isotopic study of spinel-hibonite inclusions. *Geochim. Cosmochim. Acta* **184**, 151–172.

Krawczynski M. J., Sutton S. R., Grove T. L. and Newville M. (2009) Titanium oxidation state and coordination in the lunar high-Ti glass source mantle. The 40th Lunar and Planetary Science Conference.

Leitzke F. P., Fonseca R. O. C., Göttlicher J., Steininger R., Jahn S., Prescher C. and Lagos M. (2018) Ti K-edge XANES study on the coordination number and oxidation state of Titanium in pyroxene, olivine, armalcolite, ilmenite, and silicate glass during mare basalt petrogenesis. *Contrib. to Mineral. Petrol.* **173**, 103.

Lejaeghere K., Bihlmayer G., Bjorkman T., Blaha P., Blugel S., Blum V., Caliste D., Castelli I. E., Clark S. J., Dal Corso A., de Gironcoli S., Deutsch T., Dewhurst J. K., Di Marco I., Draxl C., Du ak M., Eriksson O., Flores-Livas J. A., Garrity K. F., Genovese L., Giannozzi P., Giantomassi M., Goedecker S., Gonze X., Granas O., Gross E. K. U., Gulans A., Gygi F., Hamann D. R., Hasnip P. J., Holzwarth N. A. W., Iu an D., Jochym D. B., Jollet F., Jones D., Kresse G., Koepernik K., Kucukbenli E., Kvashnin Y. O., Locht I. L. M., Lubeck S., Marsman M., Marzari N., Nitzsche U., Nordstrom L., Ozaki T., Paulatto L., Pickard C. J., Poelmans W., Probert M. I. J., Refson K., Richter M., Rignanese G.-M., Saha S., Scheffler M., Schlipf M., Schwarz K., Sharma S., Tavazza F., Thunstrom P., Tkatchenko A., Torrent M., Vanderbilt D., van Setten M. J., Van Speybroeck V., Wills J. M., Yates J. R., Zhang G.-X. and Cottenier S. (2016) Reproducibility in density functional theory calculations of solids. *Science* **351**, aad3000–aad3000.

Leya I., Schönbächler M., Krähenbühl U. and Halliday A. N. (2009) New titanium isotope data for allende and efremovka CAIs. *Astrophys. J.* **702**, 1118–1126.

Leya I., Schönbächler M., Wiechert U., Krähenbühl U. and Halliday A. N. (2008) Titanium isotopes and the radial heterogeneity of the solar system. *Earth Planet. Sci. Lett.* **266**, 233–244.

Li X. and Liu Y. (2011) Equilibrium Se isotope fractionation parameters: A first-principles study. *Earth Planet. Sci. Lett.* **304**, 113–120.

Li Y., Wang W., Huang S., Wang K. and Wu Z. (2019) First-principles investigation of the concentration effect on equilibrium fractionation of K isotopes in feldspars. *Geochim. Cosmochim. Acta* **245**, 374–384.

Lodders K. (2003) Solar system abundances and condensation temperatures of the elements. *Sci. York* **591**, 1220–1247.

McDonough W. F. and Sun S. -s. (1995) The composition of the Earth. *Chem. Geol.* **120**, 223–253.

Méheut M., Lazzeri M., Balan E. and Mauri F. (2009) Structural control over equilibrium silicon and oxygen isotopic fractionation: A first-principles density-functional theory study. *Chem. Geol.* **258**, 28–37.

Millet M. A. and Dauphas N. (2014) Ultra-precise titanium stable isotope measurements by double-spike high resolution MC-ICP-MS. *J. Anal. At. Spectrom.* **29**, 1444–1458.

Millet M., Dauphas N., Greber N. D., Burton K. W., Dale C. W., Debret B., Macpherson C. G., Nowell G. M. and Williams H. M. (2016) Titanium stable isotope investigation of magmatic processes on the Earth and Moon. *Earth Planet. Sci. Lett.* **449**, 197–205.

Momma K. and Izumi F. (2008) VESTA : a three-dimensional visualization system for electronic and structural analysis. *J. Appl. Crystallogr.* **41**, 653–658.

Perdew J. P. and Zunger A. (1981) Self-interaction correction to density-functional approximations for many-electron systems. *Phys. Rev. B* **23**, 5048–5079.

Portillo-Vélez N. S., Olvera-Neria O., Hernández-Pérez I. and Rubio-Ponce A. (2013) Localized electronic states induced by oxygen vacancies on anatase TiO_2 (101) surface. *Surf. Sci.* **616**, 115–119.

Proyer A., Habler G., Abart R., Wirth R., Krenn K. and Hoinkes G. (2013) TiO_2 exsolution from garnet by open-system precipitation: evidence from crystallographic and shape preferred orientation of rutile inclusions. *Contrib. to Mineral. Petrol.* **166**, 211–234.

Putirka K. (2016) Amphibole thermometers and barometers for igneous systems and some implications for eruption mechanisms of felsic magmas at arc volcanoes. *Am. Mineral.* **101**, 841–858.

Putirka K. D. (2008) Thermometers and Barometers for Volcanic Systems. *Rev. Mineral. Geochemistry* **69**, 61–120.

Qian W., Wang W., Zou F. and Wu Z. (2018) Elasticity of Orthoenstatite at High Pressure and Temperature: Implications for the Origin of Low VP/VS Zones in the Mantle Wedge. *Geophys. Res. Lett.* **45**, 665–673.

Richet P., Bottinga Y. and Javoy M. (1977) A Review of Hydrogen, Carbon, Nitrogen,

Oxygen, Sulphur, and Chlorine Stable Isotope Fractionation Among Gaseous Molecules. *Annu. Rev. Earth Planet. Sci.* **5**, 65–110.

Rustad J. R. and Yin Q.-Z. (2009) Iron isotope fractionation in the Earth's lower mantle. *Nat. Geosci.* **2**, 514–518.

Samat M. H., Ali A. M. M., Taib M. F. M., Hassan O. H. and Yahya M. Z. A. (2016) Hubbard U calculations on optical properties of 3d transition metal oxide TiO_2. *Results Phys.* **6**, 891–896.

Schauble E. A. (2011) First-principles estimates of equilibrium magnesium isotope fractionation in silicate, oxide, carbonate and hexaaquamagnesium(2+) crystals. *Geochim. Cosmochim. Acta* **75**, 844–869.

Schauble E., Rossman G. R. and Taylor H. P. (2004) Theoretical estimates of equilibrium chromium-isotope fractionations. *Chem. Geol.* **205**, 99–114.

Simon J. I., Jordan M. K., Tappa M. J., Schauble E. A., Kohl I. E. and Young E. D. (2017) Calcium and titanium isotope fractionation in refractory inclusions: Tracers of condensation and inheritance in the early solar protoplanetary disk. *Earth Planet. Sci. Lett.* **472**, 277–288.

Simon S. B. and Sutton S. R. (2017) Valence of Ti, V, and Cr in Apollo 14 aluminous basalts 14053 and 14072. *Meteorit. Planet. Sci.* **52**, 2051–2066.

Simon S. B., Sutton S. R. and Grossman L. (2016) The valence and coordination of titanium in ordinary and enstatite chondrites. *Geochim. Cosmochim. Acta* **189**, 377–390.

Simon S. B., Sutton S. R. and Grossman L. (2007) Valence of titanium and vanadium in pyroxene in refractory inclusion interiors and rims. *Geochim. Cosmochim. Acta* **71**, 3098–3118.

Skogby H., Halenius U., Kristiansson P. and Ohashi H. (2006) Titanium incorporation and $VITi^{3+}$ -$IVTi^{4+}$ charge transfer in synthetic diopside. *Am. Mineral.* **91**, 1794–1801.

Togo A. and Tanaka I. (2015) First principles phonon calculations in materials science. *Scr. Mater.* **108**, 1–5.

Trinquier A., Elliott T., Ulfbeck D., Coath C., Krot A. N. and Bizzarro M. (2009) Origin of Nucleosynthetic Solar Protoplanetary Disk. *Science* **374**, 374–377.

Urey H. C. (1947) The thermodynamic properties of isotopic substances ed. S.-I. Karato. *J. Chem. Soc.*, 562.

Vanderbilt D. (1990) Soft self-consistent pseudopotentials in a generalized eigenvalue formalism. *Phys. Rev. B* **41**, 7892–7895.

Wang W., Qin T., Zhou C., Huang S., Wu Z. and Huang F. (2017a) Concentration effect on equilibrium fractionation of Mg-Ca isotopes in carbonate minerals: Insights from first-principles calculations. *Geochim. Cosmochim. Acta* **208**, 185–197.

Wang W. and Wu Z. (2018) Elasticity of Corundum at High Pressures and Temperatures: Implications for Pyrope Decomposition and Al-Content Effect on Elastic Properties of Bridgmanite. *J. Geophys. Res. Solid Earth* **123**, 1201–1216.

Wang W., Zhou C., Liu Y., Wu Z. and Huang F. (2019) Equilibrium Mg isotope fractionation among aqueous Mg^{2+}, carbonates, brucite and lizardite: Insights from first-principles molecular dynamics simulations. *Geochim. Cosmochim. Acta* **250**, 117–129.

Wang W., Zhou C., Qin T., Kang J., Huang S., Wu Z. and Huang F. (2017b) Effect of Ca content on equilibrium Ca isotope fractionation between orthopyroxene and clinopyroxene. *Geochim. Cosmochim. Acta* **219**, 44–56.

Wark D. A. and Watson E. B. (2006) TitaniQ: a titanium-in-quartz geothermometer. *Contrib. to Mineral. Petrol.* **152**, 743–754.

Watson E. B., Wark D. A. and Thomas J. B. (2006) Crystallization thermometers for zircon and rutile. *Contrib. to Mineral. Petrol.* **151**, 413–433.

Wentzcovitch R. M. (1991) Invariant molecular-dynamics approach to structural phase transitions. *Phys. Rev. B* **44**, 2358–2361.

Williams C. D., Janney P. E., Hines R. R. and Wadhwa M. (2016) Precise titanium isotope compositions of refractory inclusions in the Allende CV3 chondrite by LA-MC-ICPMS. *Chem. Geol.* **436**, 1–10.

Wu Z., Huang F. and Huang S. (2015) Isotope fractionation induced by phase transformation: First-principles investigation for Mg_2SiO_4. *Earth Planet. Sci. Lett.* **409**, 339–347.

Young E. D., Tonui E., Manning C. E., Schauble E. and Macris C. A. (2009) Spinel–olivine magnesium isotope thermometry in the mantle and implications for the Mg isotopic composition of Earth. *Earth Planet. Sci. Lett.* **288**, 524–533.

Zhang J., Dauphas N., Davis A. M., Leya I. and Fedkin A. (2012) The proto-Earth as a significant source of lunar material. *Nat. Geosci.* **5**, 251–255.

Zhang J., Dauphas N., Davis A. M. and Pourmand A. (2011) A new method for MC-ICPMS measurement of titanium isotopic composition: Identification of correlated isotope anomalies in meteorites. *J. Anal. At. Spectrom.* **26**, 2197–2205.

Zhang J., Huang S., Davis A. M., Dauphas N., Hashimoto A. and Jacobsen S. B. (2014) Calcium and titanium isotopic fractionations during evaporation. *Geochim. Cosmochim. Acta* **140**, 365–380.

Appendix

Click here to download Appendix: Supplementary materials-revised-0901.docx

Data in Brief

Click here to download Data in Brief: relaxed_structures.zip

Declaration of interests

The authors declare that they have no known competing financial interests or personal relationships that could have appeared to influence the work reported in this paper.